P-T-D evolution of the southeast Passo Feio Complex and the meaning of the Caçapava Lineament, Dom Feliciano Belt, southernmost Brazil

Elisa Oliveira da Costa [1*] - **elisa.oliveira.da.costa@gmail.com**

Maria de Fátima Bitencourt [1] - fatimab@ufrgs.br

Tonje Tennholm [2] - tonjetk@hotmail.com

Jiří Konopásek [2,3] - jiri.konopasek@uit.no

Thayse de Franceschi Moita [4] – thaysemoita@hotmail.com[1]

[1]Programa de Pós-graduação em Geociências, Instituto de Geociências, Universidade Federal do Rio Grande do Sul, Av. Bento Gonçalves, 9500, Porto Alegre, 91500-000, RS, Brasil.

[2] Department of Geosciences, UiT The Arctic University of Norway, Postboks 6050 Langnes, 9037 Tromsø, Norway.

[3] Czech Geological Survey, Klárov 3, 118 21 Prague, Czech Republic

[4] Instituto de Geociências, Universidade Federal do Rio Grande do Sul, Av. Bento Gonçalves, 9500, Porto Alegre, 91500-000, Porto Alegre, Brazil

[*] Corresponding Author

Abstract

Metamorphic–deformation paths and interpretations of regional structures are essential for the understanding of how orogens evolve. While in active orogens, structures can be easily mapped for hundreds of kilometres, regional structures in ancient mountain belts may appear only as subsurface geophysical data. In this paper, we constrain the metamorphic–deformation history of the southeastern part of the Passo Feio Complex located in the Neoproterozoic Dom Feliciano Belt in southernmost Brazil. The complex is crosscut by a block-limiting structure defined by magnetometric data, the Caçapava Lineament. Our petrographic interpretations and thermodynamic modelling of pelitic schists of the Passo Feio Complex indicate the beginning of garnet growth at ca. 530–550 ºC and 3–4.3 kbar during D_1, and metamorphic peak at ca. 560–570 ºC and 5–5.5 kbar (M_1), during progression to D_2. After M_1 (~17–19 km depth), the complex was exhumed to at least 14 km (~4kbar) depth, as the contact metamorphism by the Caçapava Granite (ca. 562 Ma) produced andalusite. The correlation of D_3 structures of the Passo Feio Complex (S_3 and L_3), magmatic structures in the Caçapava Granite, orientation of geophysical anomalies in the region and kinematics of S_3 corroborate the interpretation of the Caçapava Lineament as a dextral shear zone. Due to the location of anomalies and previous three-dimensional modelling of the granitic body, we interpret that a curved ENE to NS branch of the NE-striking Caçapava Shear Zone is responsible for the accommodation of the Caçapava Granite. Lastly, we discuss the regional implications of such interpretation, which brings up the question of block-limiting character of the Caçapava Shear Zone and the geotectonic position of the Passo Feio Complex.

Keywords: Thermodynamic modelling; Perple_X; Caçapava Shear Zone; Dom Feliciano Belt;

Introduction

The geometry and significance of regional structures developed in metamorphic rocks are essential to construct models. They permit to establish boundaries of tectonic blocks and investigate how they evolved. In recent orogens, regional structures and domain boundaries are easily mapped for more than 1000 km, e.g. Main Frontal Thrust in the Himalayas (e.g., Gansser, 1964; Nakata, 1989; Bilham et al., 1998). In ancient orogens, however, description and recognition of regional structures may have to rely only on subsurface data, as they may be almost completely covered by post-collisional basin sediments.

The Neoproterozoic Dom Feliciano Belt in southernmost Brazil has a typical case of regional structure deduced from an incomplete dataset. The eastern boundary of its westernmost domain, the São Gabriel Block, is known as the Caçapava Lineament (CL - Fig. 1a), originally described as a straight and continuous lineament marked by an aeromagnetic discontinuity by Costa (1997). This structure was interpreted to represent a suture and terrain boundary, resulting from the closure of an oceanic basin (Fernandes et al., 1995a, Costa, 1997). In recent papers, it is represented as a shear zone on regional maps (e.g. Chemale, 2000, Philipp et al., 2013, 2016), but no information is given about its geometry, kinematics or genetic conditions. The possibility of a dextral transcurrent shear zone in this region was pointed out by Costa et al. (1995) as part of a model to explain the emplacement of the Caçapava Granite at ca. 562 Ma, but the authors give no further information. Therefore, despite different references to its existence, the Caçapava Shear Zone has never received enough attention to correctly position it on regional maps or discuss its kinematics or structural development. Consequently, its role as terrane boundary or domain divider remains under questioning.

In this paper, we present data obtained from the southeastern part of the Passo Feio Complex, where it is crosscut by the Caçapava Lineament. The study aims at constraining the metamorphic path of metapelites and understanding their deformation. We use field structural data, petrographic, microstructural and thermodynamic modelling data to discuss the metamorphic-deformation history of the complex and the geological meaning of the Caçapava Lineament in the regional structural framework.

Geological Setting

Regional Geology

The Neoproterozoic Dom Feliciano Belt (DFB) in southernmost Brazil and Uruguay represents the South American portion of the ca. 1200 km long Dom Feliciano–Kaoko–Gariep orogenic system formed during the Neoproterozoic assembly of West Gondwana (Oriolo et al., 2017; Konopásek et al., 2018 – Fig. 1a). The Dom Feliciano Belt is adjacent to the Luis Alves Craton in the north and the Nico Perez Terrane and Rio de La Plata Craton in the southwest (Oyhantçabal et al., 2011). Some Archean and Paleoproterozoic basement inliers comprising mainly orthogneisses are exposed throughout the DFB, partly covered by metamorphosed pre-orogenic deposits of Mesoproterozoic–Tonian age (Oriolo et al., 2019; Percival et al., 2021), as well as syn- to post-collisional volcano-sedimentary deposits of Ediacaran to Cambrian age (Pertille et al., 2017; Höfig et al., 2018; Almeida et al., 2010, 2012). The DFB in southern Brazil is usually subdivided into five tectonic domains delimited by regional lineaments (Fernandes et al., 1995a; 1995b; Hartmann et al., 2016; De Toni et al., 2021; Basei et al., 2011 – Fig. 1b).

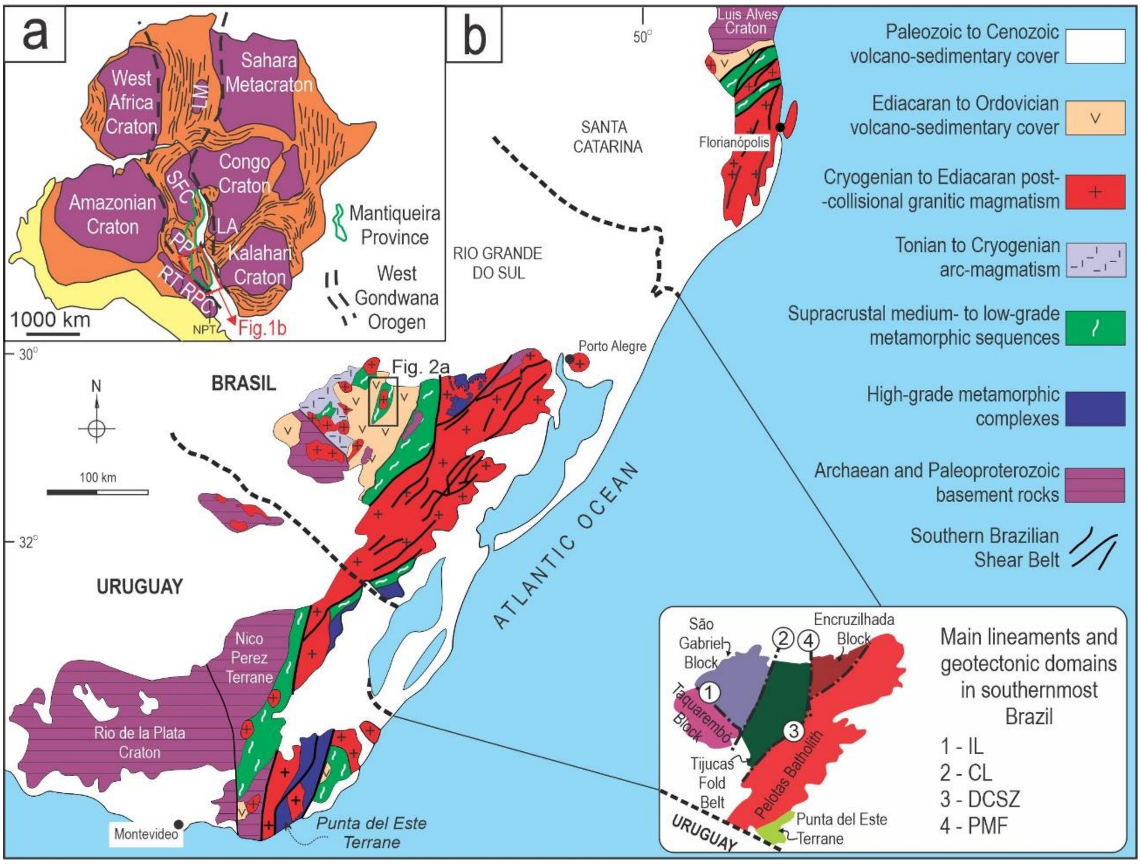

Fig. 1. a) Geotectonic reconstruction of West Gondwana (modified from Oriolo et al., 2017; Will et al., 2019) with the area of figure 1b indicated. LM – Latea Metacraton;

SFC – São Francisco Craton; RT- Rio Tebicuary Craton; PP – Paranapanema Craton; LA – Luis Alves Craton; NPT – Nico Peres Terrane; RPC – Rio de la Plata Craton. b) Geotectonic map of Dom Feliciano Belt and surrounding Archean and Paleoproterozoic basement rocks (modified from Bitencourt and Nardi, 2000; Ramos et al., 2018; Will et al., 2019). IL – Ibaré Lineament; CL – Caçapava Lineament; DCSZ – Dorsal de Canguçu Shear Zone; PMF – Passo do Marinheiro Fault. Area of figure 2 indicated.

NO COLOR IN PRESS

The westernmost tectonic domain is the São Gabriel Block, which is bounded by the NW-trending Ibaré Lineament and the NNE-trending Caçapava Lineament (CL – Fig. 1b inset). The oldest rocks of the São Gabriel Block are attributed to the so-called Passinho event (ca. 930 – 880 Ma), a period of accretion of an intra-oceanic arc recorded in ophiolites (Arena et al., 2016) and metadiorite (Leite et al., 1998). Ophiolite obduction would have taken place at ca. 790 Ma (Arena et al., 2016). Calc-alkaline metatuffs and meta-conglomerates (Gubert et al., 2016), orthogneisses (Leite et al., 1998; Hartmann et al., 2011) and metavolcanic rocks (Machado et al., 1990; Remus et al., 1999) with ages of ca. 770 to 720 Ma are considered by Philipp et al. (2018) as associated with another period of magmatic arc formation called the São Gabriel event. The orthogneisses were subsequently intruded by a ca. 705 to 690 Ma tonalite–diorite igneous suite (Babinski et al., 1996; Hartmann et al., 2011). Ediacaran post-collisional granites are also common in this domain.

The central-western tectonic domain is the foreland Tijucas Fold Belt (Hasui et al., 1975 – green domain of Fig. 1b inset), bounded to the west by the CL and to the east by the Dorsal de Canguçu Shear Zone (DCSZ) and Passo do Marinheiro Fault (PMF). This domain is interpreted as a deformed and metamorphosed volcano-sedimentary basin (e.g. Gruber et al., 2016; Pertille et al., 2015; Höfig et al., 2017) with periods of volcanic activity at ca. 780 Ma (Saalman et al., 2011; Martil et al., 2017) and from ca. 600 to 580 Ma (Höfig et al., 2017). Metamorphic and deformation events occurred at ca. 650 Ma (Lenz 2006) and ca. 570 Ma (Höfig et al., 2017; Battisti et al., 2018). Past and recent works have shown that in southernmost Brazil, the Tijucas Fold Belt comprises two tectonically imbricated sequences (Jost & Bitencourt 1980; Höfig et al., 2017; Battisti et al., 2018). Therefore, the metamorphic complex that comprises the Tijucas Fold Belt in Rio Grande do Sul state (green domain of Fig. 1b inset), the Porongos Metamorphic Complex (PMC), can be divided into two domains referred to as Porongos I and Porongos II (Höfig et al., 2017; Battisti et al., 2018). Peak metamorphic conditions registered in the PMC are ca. 560–590ºC and 5.8–6.3 kbar with retrograde reworking at 550 ºC and 2.7 kbar (Lenz, 2006; De Toni et al., 2021).

To the east of the DCSZ, Cryogenian to Ediacaran post-collisional granitic rocks form the Florianópolis–Pelotas–Aiguá Batholith (Fig 1b). Emplacement of these rocks between ca. 640 and 580 Ma (Bitencourt & Nardi, 2000; Philipp et al., 2002) was controlled by an anastomosing array of shear zones known as the Southern Brazilian Shear Belt (Bitencourt & Nardi, 2000).

The central-northeastern portion of the Florianópolis–Pelotas–Aiguá Batholith is called the Encruzilhada Block (EB), first defined by Jost & Hartmann (1984). Recently, the evolution of this area was re-interpreted by Battisti et al. (2018), Costa et al. (2020) and De Toni et al. (2021) in terms of westward oblique thrusting of a granulitic complex over the Tijucas Fold Belt. This event was followed by emplacement of granitic rocks along the foreland–hinterland interface and voluminous post-collisional magmatism within the Encruzilhada Block and the rest of the Pelotas Batholith (ca. 640–578 Ma – Bitencourt et al., 2016; Nardi et al., 2008; Rivera, 2019; Padilha et al., 2019).

The easternmost tectonic domain of the Dom Feliciano Belt is the Punta del Este Terrane, which outcrops mainly in Uruguay, but has recently been extended into southernmost Brazil (Ramos et al., 2018). The limit with the batholith is a NNE-striking shear zone (Preciozzi et al., 1999). Similar to the Encruzilhada Block, the Punta del Este Terrane comprises high-grade complexes with ca. 780–800 Ma calc-alkaline igneous protolith (Lenz et al., 2011; Masquelin et al., 2012), associated either with a magmatic arc setting (Lenz et al. 2013; Koester et al., 2016; Martil et al., 2017; De Toni et al., 2020) or with rift-related magmatism (Konopasek et al., 2018; 2020; Will et al., 2019). The Punta del Este Terrane shows a metamorphic peak at ca. 655-632 Ma (Will et al., 2019) and partial melting at ca. 654-630 Ma (Oyhantçabal et al., 2009; Lenz et al., 2011; Will et al., 2019).

Passo Feio Complex

The Passo Feio Complex (PFC) is situated near the eastern boundary of the São Gabriel Block represented by the Caçapava Lineament (CL - Fig. 2a), which runs through its southeastern portion (Fig. 2b). The PFC consists of metapelitic schists and phyllites, amphibole-bearing rocks such as amphibolites, metagabbros and amphibole schists, acid to intermediate metavolcanoclastic rocks, and subordinate magnesian schists and marble lenses and metavolcanic rocks (Bitencourt, 1983a, b). The PFC is arranged in a double-plunging antiformal structure with subhorizontal axis plunging both to NNE and SSW. At the centre of this structure, the calc-alkaline Caçapava Granite intruded the PFC at 562 ± 8 Ma (SHRIMP U–Pb zircon - Remus et al., 2000). To the west and east, the complex is covered by Ediacaran to Ordovician volcano-sedimentary sequences of the Camaquã Basin (Paim et al., 2014 - Fig. 2a).

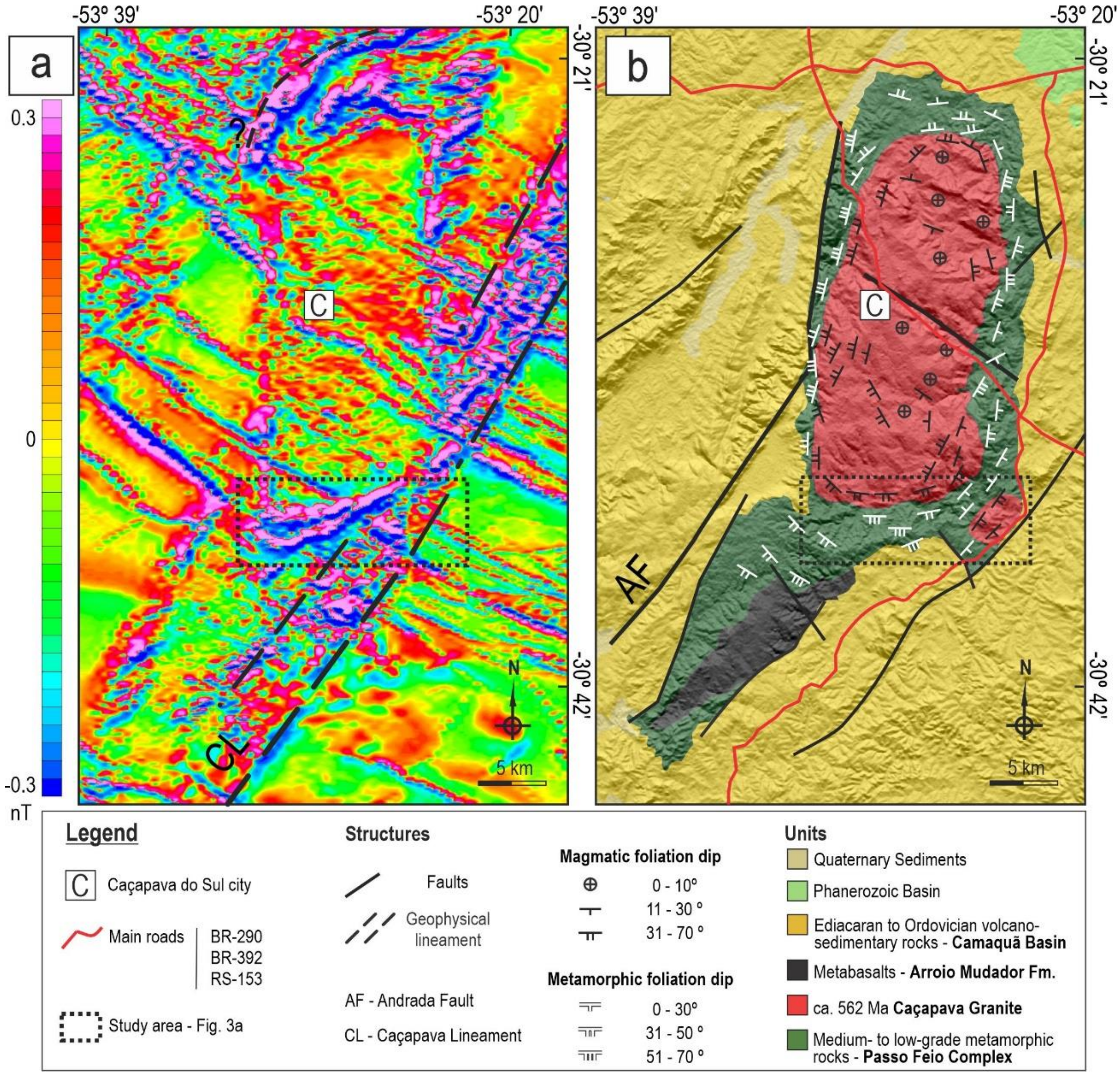

Fig. 2. a) Aerogeophysical map of the study area (first derivate), with geophysical structures indicated. Modified from Wildner et al. (2006) and CPRM (2010). b) Geological map of the Passo Feio Complex with main structures of the complex and the Caçapava Granite. Modified from Bitencourt (1983a), UFRGS (1998), Nardi & Bitencourt (1989) and Wildner et al. (2006).

NO COLOR IN PRESS

Acid metavolcanic rocks are rare and have not yet been characterised in terms of geochemistry and geochronology, while amphibole-bearing rocks were studied by Bitencourt & Hartmann (1984a, b) and Bicalho et al. (2019). The data of Bitencourt & Hartmann (1984a, b) refer to the northern and southern parts of the complex. They suggest that most samples are ortho-amphibolites, either volcanic or volcano-sedimentary in origin, part of them tholeiitic and part alkaline. Bicalho et al. (2019)

studied the northern part of the complex, and found amphibolites of basaltic-andesitic compositions with predominantly tholeiitic affinity.

Two metamorphic events were described in the PFC by Bitencourt (1983a, b). M_1 reached the staurolite zone, and the presence of andalusite was taken to indicate Buchan-type metamorphism, while retrogressive M_2 records biotite zone conditions. The same author interpreted the emplacement of the Caçapava Granite to have been late relative to M_2. Hartmann et al. (1990) argued that the presence of andalusite, together with the distribution of Al and Ti in amphibole, and weak chemical zonation of staurolite, suggested low-pressure metamorphism. Moreover, Bicalho et al. (2019) interpreted chemical zonation registered in amphiboles as indicative of progressive metamorphism, with no record of retrogressive M_2. Bitencourt (1983a, b) pointed out a metamorphic zonation towards the north, where anchimetamorphic rocks are found. In addition, Borba et al. (2002) reported Triassic ages for a NW-striking normal fault, which would have been responsible for the uplift of the southern block relative to the northern one, and would further account for the lower grade rocks observed in the north.

Available geochronological data on the PFC are rather limited and imprecise. Age values for M_1 were acquired in narrow zircon rims from metapelite or para-amphibolite, and range from 710 to 670 Ma, with high associated error (Remus et al., 2000, Souza 2020). The age of M_2 is interpreted from its close relationship to the emplacement of the Caçapava Granite (Bitencourt, 1983b; Nardi & Bitencourt, 1989) dated at 562 ± 8 Ma (SHRIMP U-Pb zircon – Remus et al., 2000).

Three deformation events were described in the PFC by Bitencourt (1983a, b). The first event (D_1) is observed in thin sections as rotated inclusion trails in pre-kinematic porphyroblasts relative to S_2 and transposed microfolds between S_2 planes. D1 is interpreted from structures preserved inside quartz lenses and recumbent isoclinal folds in marbles and volcano-sedimentary rocks at mesoscale. The second event (D_2) developed the main foliation S_2, whose geometry was modified by the last deformation event, D_3. Finally, D_3 generated cm- to km-size folds and S_3 crenulation cleavage that predominate in the region and make up the antiformal structure of the PFC.

Materials and Methods

Imaging of garnet chemical zonation was made with Scanning Electron Microscope (SEM) Zeiss Merlin VP Compact in the SEM Laboratory of the Health Sciences Faculty, UiT The Arctic University of Norway, Tromsø. Analytical conditions were 20 kV acceleration voltage and 120 μm beam aperture. Bulk composition of pelitic schist and phyllite samples were obtained by X-ray fluorescence method at both the Department of Geosciences of UiT, The Arctic University of Norway in Tromsø, and the Bureau Veritas laboratories, Canada, for quality control. Mineral chemistry was analysed with a CAMECA SX100 electron microprobe with five spectrometers and operating acceleration voltage of 15 kV and beam current of 15 nA at the University of Oslo.

Thermodynamic modelling of metamorphic evolution of pelitic schists and phyllites was made using the software package Perple_X, version 6.8.7 (Connoly 2005; 2009) utilising the internally consistent thermodynamic dataset of Holland & Powell (1998, upgraded in 2004). Solution models for staurolite, garnet, white mica, biotite, chlorite, chloritoid, cordierite and ilmenite are from White et al. (2014), while the model of Fuhrman & Linsdley (1988) was used for feldspar. P–T pseudosections were first constructed based on the major element bulk chemistry of the studied samples, and chemical mineral data were used to plot the corresponding isopleths. Garnet core composition was used to constrain the P–T conditions of the beginning of garnet growth. The composition of other matrix minerals and the garnet rim constrain the peak P–T conditions. Since garnet is abundant and displays a strong chemical zonation, a 1-d fractionation routine was used to estimate effective system composition to stabilise the matrix mineral assemblage. Therefore, the peak metamorphic conditions were estimated in pseudosections calculated with fractionated bulk composition.

Results

Structural Framework

As described by Bitencourt (1983a, b), S_2 is the PFC main foliation, which has formed parallel to axial planes of the recumbent isoclinal folds of the first foliation S_1. Thus, it may not always be possible to distinguish relict S_1 from S_2, as they tend to be parallel. As can be seen in figure 2, S_2 strikes contour the Caçapava Granite. However, our field data show a zone in the east where S_3 is the main foliation (Fig. 3a).

S_2 poles (Fig. 3b) are dispersed and lie along a broad girdle that results from large-scale folding (F_3) during D_3. Stretching lineations observed in quartz aggregates parallel to S_2 are interpreted as L_2. They are scarce and plunge towards various directions, possibly due to later D_3 folding. The girdle formed by poles to S_2 indicates a sub-horizontal, NE-plunging fold axis, which is compatible with the orientation of D_3 crenulation axes (L_B) developed on S_2.

The interleaving of mostly cm- to m-thick pelitic schists and amphibolites, but also of metavolcanic and metavolcano-sedimentary rocks, chlorite and talc schists, is visible at outcrop scale. As previously mentioned by Bitencourt (1983a; 1983b), this interleaving is controlled by S_2, which represents regionally folded, but originally subhorizontal foliation planes. Therefore, the separation of compositional layers at the map scale is not realistic. S_2 is best developed in pelitic schists, marked by lepidoblastic texture of micas, and in amphibole-bearing rocks where either the nematoblastic texture of amphiboles and/or development of compositional bands also mark S_2.

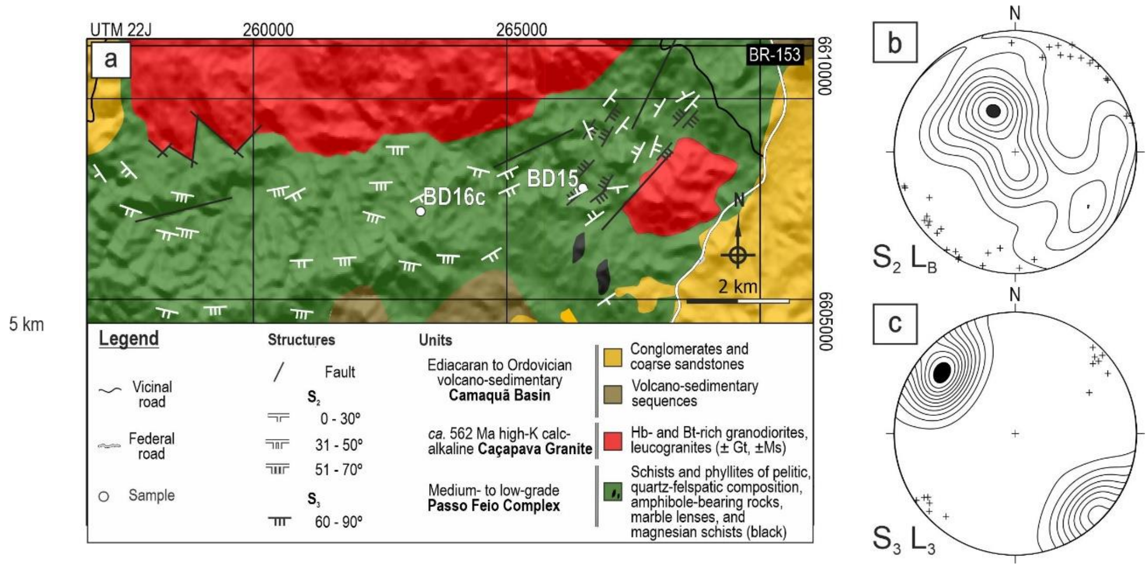

Fig. 3. a) Geological map of the study area with location of modelled samples. S_2 foliation orientations are from this work and Bitencourt (1983a, b), while S_3 are all from this work. b) Lower hemisphere, equa-area stereographic plots with contoured poles to the main foliation S_2 (n=56), with contoured intervals of 12 and crenulation axis L_B (n=36). c) Lower hemisphere equal area stereographic plots with contoured poles to S_3 (n=82), contour intervals of 10 and stretching lineation, L_3 (n=14).

NO COLOR IN PRESS

Folding of S_2 leads to axial-planar, subvertical, NE-striking S_3 crenulation cleavage observed in the entire study area (Fig. 4a-b). In the eastern zone, as mentioned above, a well-developed, NE-striking subvertical foliation becomes dominant (S_3 – Fig. 3a and 3c). Therefore, some outcrops in this area were selected to be sketched in detail to assess the meaning of S_3 at the mesoscale (Fig. 5). The relatively large exposure allowed to define the width of up to 20 m for areas of dominant S_3 adjoining areas of dominant S_2. Common features found in other outcrops were also found in this outcrop as relict folded S_2 (Fig. 4c) and low-strain domains where sub-horizontal S_2 is preserved (Fig. 4d and Fig. 5). Folded quartz veins and stretched quartz veins that resemble σ-type porphyroclasts indicate clockwise rotation of S_3 along a sub-horizontal shear direction indicated by stretching lineation L_3 (Fig. 4e). Asymmetrical, rotated relicts of S_2 indicate dextral shearing along S_3 (Fig. 4f and Fig. 5). In areas where S_3 is the dominant foliation, a stretching lineation L_3 plunges at shallow angles towards NE or SW (Fig. 3c).

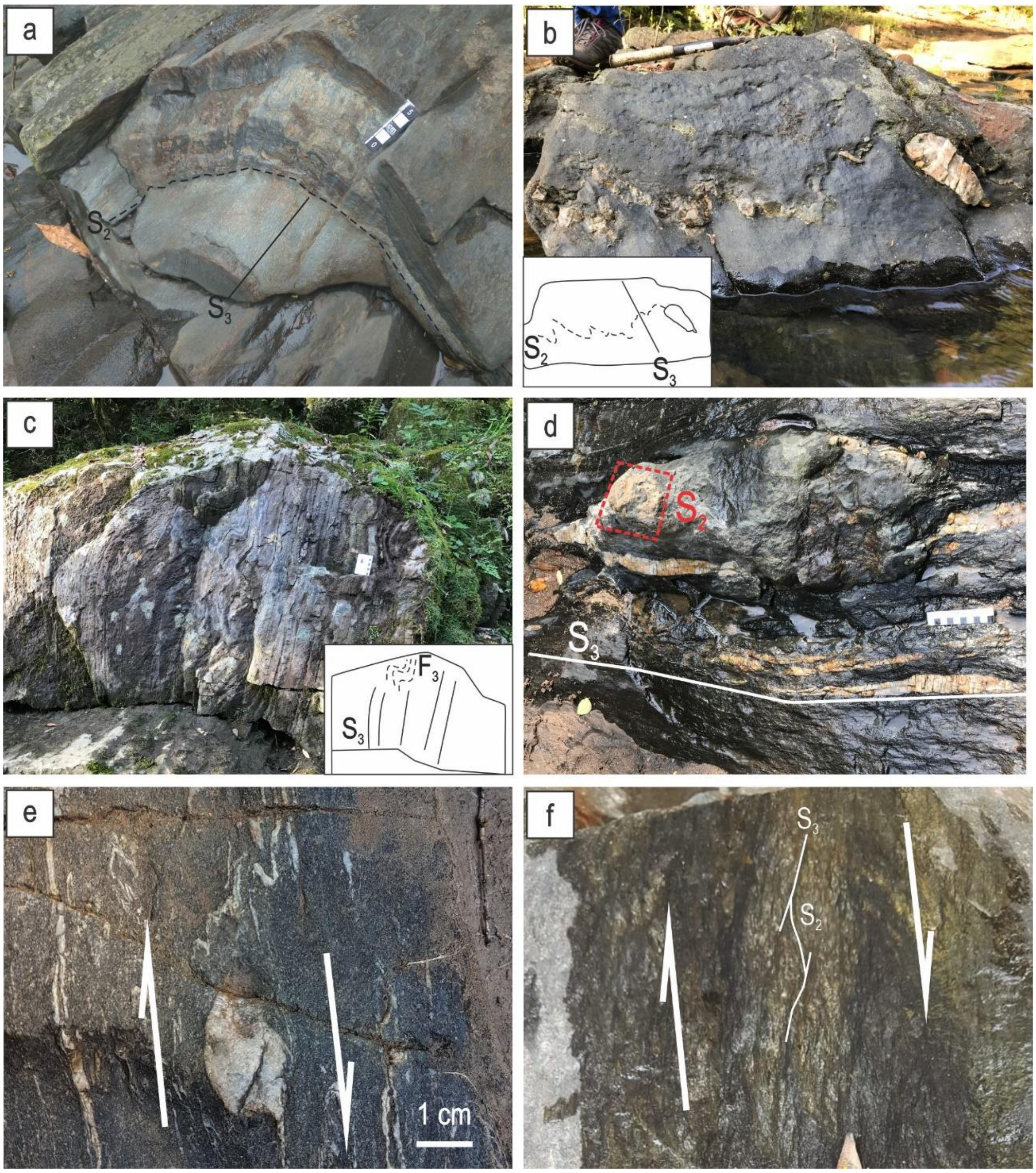

Fig. 4. Mesoscale structures observed in the study area in metapelitic schists. Figures c, d and f are from the same outcrop as Figure 5. a) Crenulated sub-horizontal S_2 preserved in more competent layers, cylindrical F_3 folds with subhorizontal axis parallel to the crenulation axis (L_B), and well-developed S_3 crenulation cleavage in less competent layers. b) Strong crenulation of S_2 and intersection of S_2 and S_3. c) Outcrop area where S_3 is the dominant foliation, with relict F_3. d) Pod of preserved subhorizontal foliation (S_2) in the area where S_3 is the main foliation (Fig. 5). e) Deformed Qz vein indicating clockwise rotation of S_3. f) Dextral drag of S_2 by S_3.

NO COLOR IN PRESS

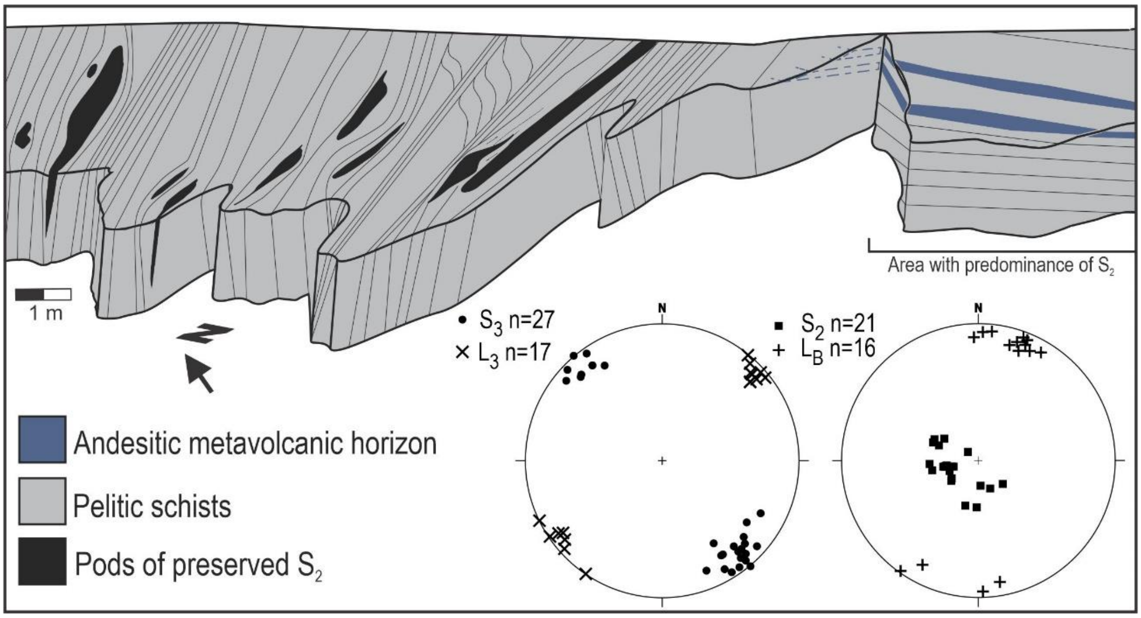

Fig. 5. Detailed outcrop sketch and measured structural data. Areas with predominant S_2 foliation (right stereogram) are next to areas of strongly-developed S_3 (left stereogram) that contain pods of preserved S_2 and where S_3 drags S_2 with dextral shear sense.

NO COLOR IN PRESS

Petrography and Microstructures

Only one of the samples studied in this work has clear evidence of S_1 represented by folded inclusion trails in staurolite porphyroblasts (Fig. 6a-b). Inclusion trails parallel to the axial planes of such folds are parallel to the matrix S_2 foliation and thus interpreted as S_2 (Fig. 6b). In these pelitic schists, the lepidoblastic texture of biotite and muscovite, with minor amounts of chlorite, and the alternation of micaceous and quartz-feldspathic domains mark S_2 (Fig.6c-d). Garnet porphyroblasts are typically subhedral to euhedral and may reach up to 5 mm. Inclusion trails in garnet porphyroblasts are typically spiralled, indicating the synkinematic character of garnet crystals. In some samples, garnet inclusion trails are straight, either parallel or perpendicular to the main external foliation, and more rarely, the inclusions are randomly oriented or absent.

Metavolcanic layers of andesitic composition show porphyroclasts of plagioclase and amphibole set in quartz-feldspathic matrix. The preferred orientation of porphyroclasts and discontinuous coarse-grained layers mark S_2 (Fig. 6e). In quartz-feldspathic phyllites, S_2 is marked by alternating layers of fine and coarse grain size (Fig. 6f), while amphibole-bearing phyllites display nematoblastic texture of amphibole alternated with layers of quartz-feldspathic composition (Fig. 6g). Amphibole-bearing rocks vary from phyllites to schists (Fig. 6h).

Samples located in the east, where S_3 is the main foliation, have distinct microstructures and textures (Fig. 7). Crenulation F_3 folds with axial-planar S_3 cleavage are better developed in this area (Fig. 7b), and as shown in figure 7a, domains of strongly-folded S_2 are found side by side with domains of well-developed subvertical foliation S_3. Observation of XZ-parallel sections of S_3-dominated samples revealed C'-type shear bands that rotate S_3 in a clockwise sense, in agreement with the kinematics indicated by the σ-type mantled clasts (Fig. 7c). Moreover, dextral drag of S_2 by S_3 is observed in ~2 mm-thick microlithons between S_3 planes (Fig. 7d-e). This shear sense is in agreement with the kinematics observed in antithetic microfractures affecting the porphyroclast, as outlined in figure 7e. The thin section in figure 7d is the only one to display two texturally different Gt crystals. Gt_1 forms up to 2 mm fractured Gt porphyroblasts, whose fractures are sealed by Qz, and Gt_2 forms ca. 0.2 mm Gt crystals, similar in size to other minerals in the matrix.

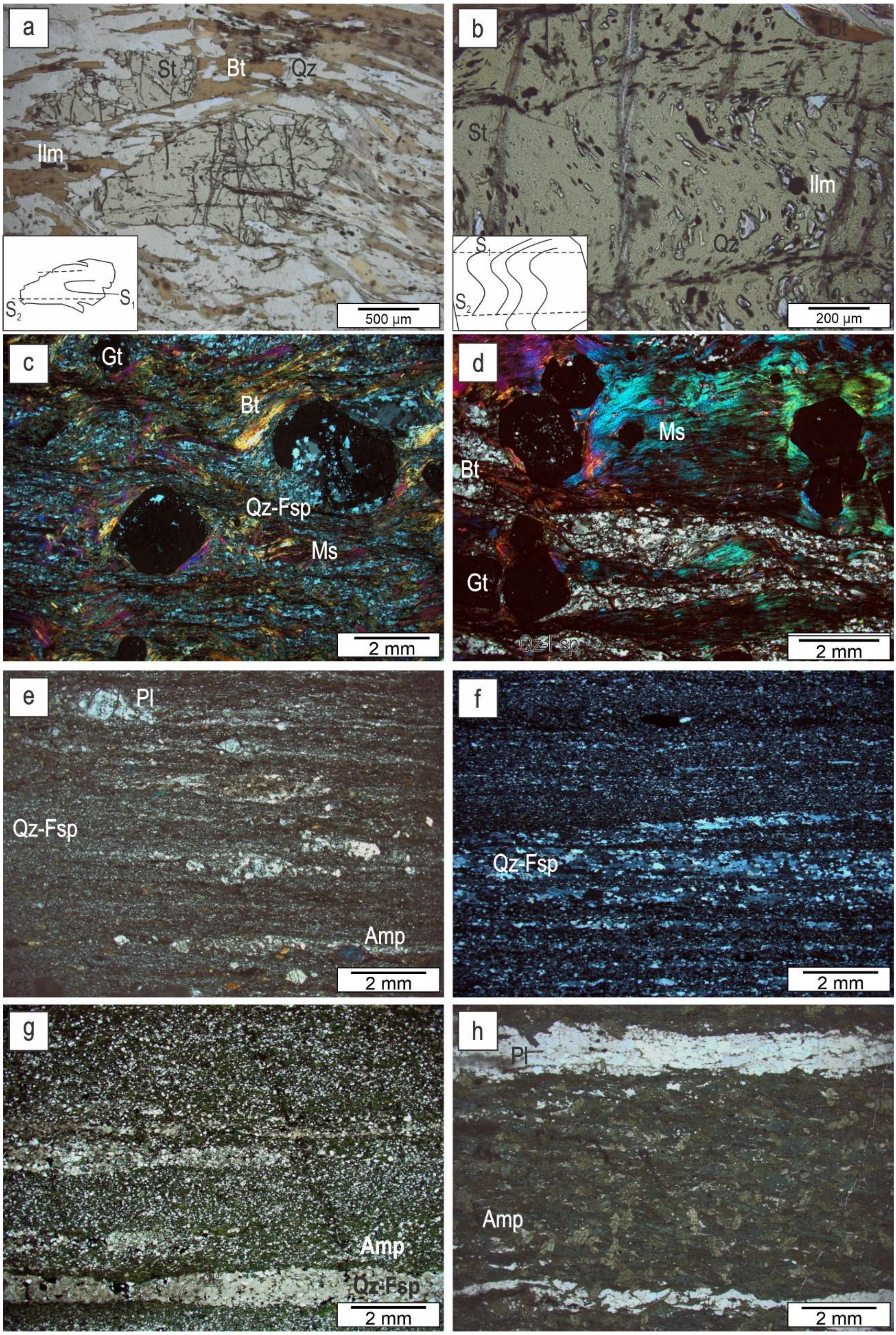

Fig. 6. Photomicrographs of different PFC rock types where S_2 is the main foliation. Matrix foliation is S_2 in all cases. a) Staurolite porphyroblast with folded internal foliation (S_1) and S_2 parallel to the external foliation. b) Staurolite porphyroblast with folded

internal foliation S_1 and axial-planar S_2. c) Garnet-biotite-muscovite schist with euhedral to subhedral, synkinematic garnet porphyroblasts set in well-developed matrix with domains of micas and quartz-feldspar. d) Garnet-biotite-muscovite schist with euhedral to subhedral garnet porphyroblasts exhibiting textural zoning of inclusions in a well-developed matrix with alternating domains of micas and quartz-feldspar. e) Andesitic metavolcanic rock with fine quartz-feldspar matrix and porphyroblasts of plagioclase and amphibole. f) Quartz-feldspar phyllite. g) Amphibole phyllite with quartz-feldspar domains. h) Amphibole schist with discontinuous plagioclase domains.

NO COLOR IN PRESS

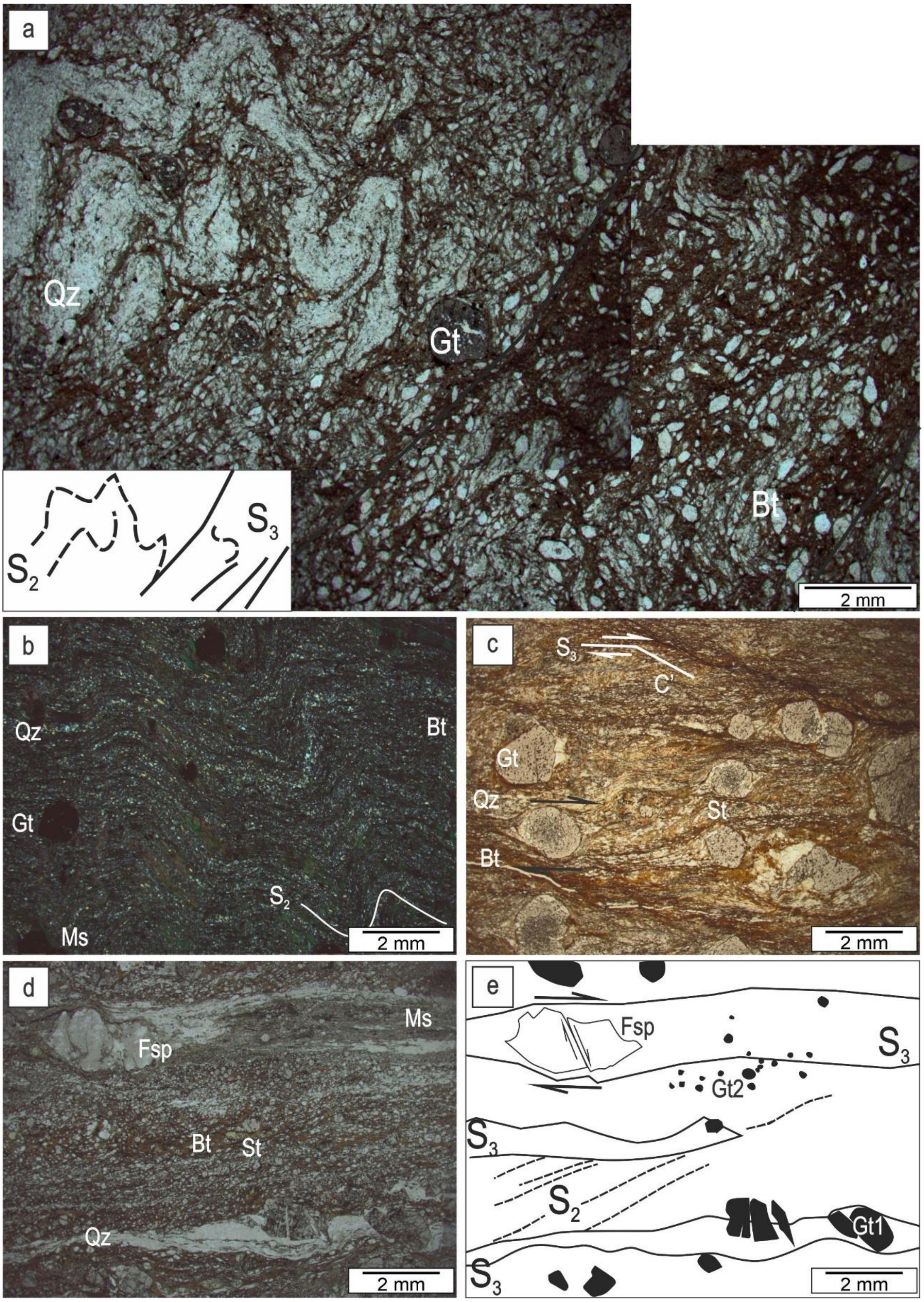

Fig. 7. Microstructures in the eastern zone of the study area, where S_3 is the main planar structure. a) Garnet-staurolite schist with strongly crenulated S_2 (left side) and S_3 as the main foliation (right side). b) Garnet-staurolite schist with strongly crenulated S_2. c) Clockwise rotation of S_3 indicated by σ-type mantled garnet porphyroblast in agreement with C'-type shear bands. d) Garnet-staurolite schist with antithetic

microfracture in K-feldspar porphyroclasts, and S_2 domains dragged dextrally by S_3. e) Sketch of photomicrograph d, where structures are indicated, as well as two textural types of Gt - Gt_1 (fractured porphyroblasts), and Gt_2 (small, clear crystals).

NO COLOR IN PRESS

Petrography of modelled samples

Two samples were selected for modelling of metamorphic conditions registered in two different lithologies, a Gt phyllite (BD16c) and a St-Gt schist (BD15) (Fig. 2b). Sample BD15 was also selected to assess the meaning of andalusite as an indicator of Buchan-type metamorphism or contact metamorphism.

Sample BD16c

Sample BD16c (22J 263274mE, 6606799mN) is a phyllite with Gt–Bt–Ms–Qz–Chl–Pl–Ilm mineral assemblage. The main foliation, S_2, is marked by lepidoblastic texture of micas (Fig. 8a). Subhedral garnet crystals are up to 0.5 mm large and correspond to 5 vol. % of the sample, while micas (30 vol. % biotite and 20 vol. % muscovite) and quartz (30 vol. %) are the main constituents of the sample. Micas of the matrix wrap around garnet crystals, implying that garnet was already present during the recrystallisation of the matrix. Rotated inclusions in garnet are represented by quartz, ilmenite and plagioclase (Fig. 8b).

With the exception of X_{Mg} that remains 0.06-0.07 throughout the crystal, garnet composition varies from core to rim. Amounts of X_{Prp} vary from 0.03 to 0.03–0.04, X_{Alm} from 0.44–0.54 to 0.57–0.61, X_{Grs} from 0.08–0.10 to 0.07–0.11 and X_{Sps} from 0.31–0.34 to 0.22–0.30. Bt has X_{Mg} of 0.35–0.40, and Si in Ms is 3.05 to 3.09 a.p.f.u. (Supplementary Table 1).

SampleBD15

Sample BD15 (22J 266342mE, 6607383mS) is a St–Gt–Bt–Ms–Chl–Ilm–Qz–Pl–And schist. Layers of medium-grained biotite and muscovite of lepidoblastic texture and discontinuous layers of quartz and plagioclase (Fig. 8c) wrap around subhedral porphyroblasts of garnet up to 1.2 mm in diameter and staurolite of ~0.4 mm in length, and mark the S_2 foliation. Garnet crystals have inclusion trails of ilmenite and quartz parallel to the external (S_2) foliation. Fine-grained chlorite is present around some garnet crystals, which is interpreted to indicate retrograde metamorphism. Rare andalusite crystals are subhedral and seem to overgrow the S_2 foliation (Fig. 8d).

Compositional zonation of garnet from core to rim is observed. The value of X_{Prp} varies from 0.04–0.07 to 0.07–0.08, X_{Alm} from 0.71–0.84 to 0.85, X_{Grs} from 0.05–0.06 to 0.03–0.04, X_{Sps} from 0.04–0.17 to 0.03–0.04, and X_{Mg} = 0.06–0.08 to 0.08–0.09. The values of X_{Mg} in St are 0.11–0.15, in Bt are 0.32–0.38, and Si in Ms equals to 3.03–3.05 a.p.f.u. (Supplementary table 1).

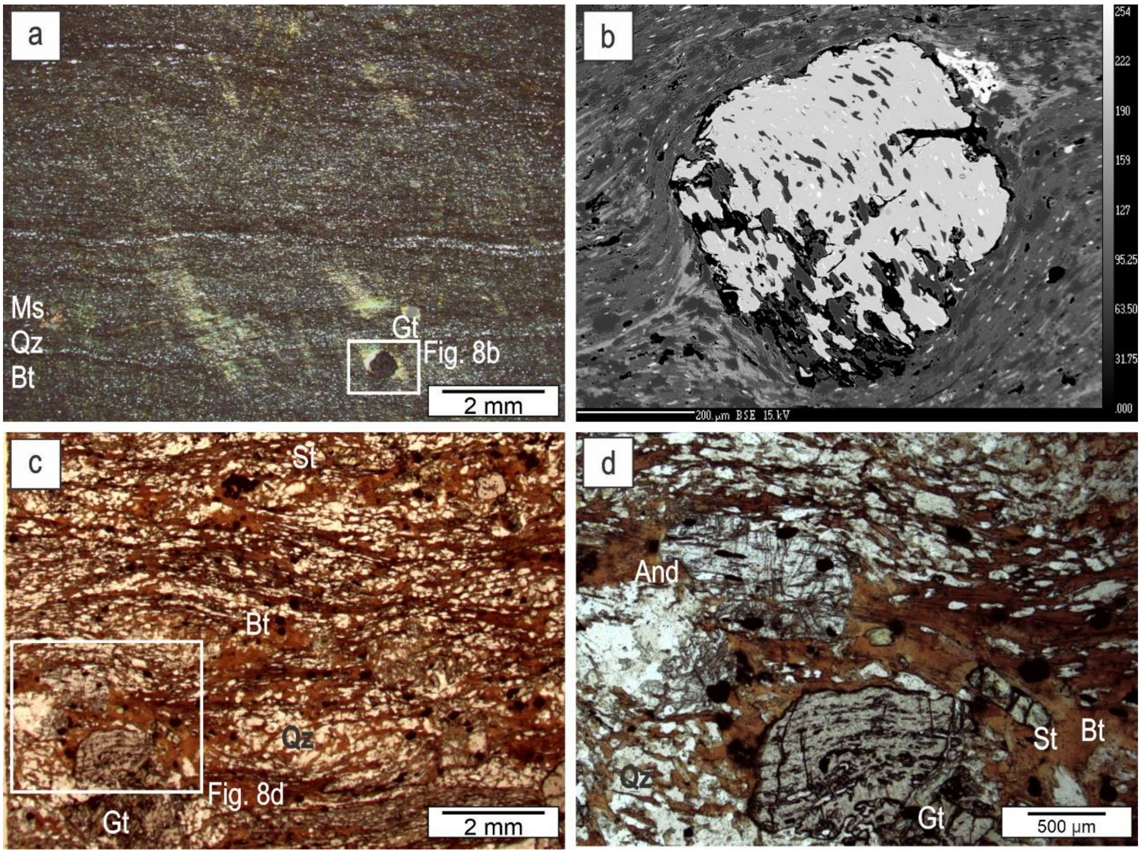

Fig. 8. a) General texture of sample BD16c with scarce synkinematic garnet set in a matrix of alternating fine domains of quartz and mica. b) SEM image of a garnet porphyroblast from sample BD16c showing spiralled inclusions. c) Photomicrograph of sample BD15 showing its general texture, defined by the lepidoblastic texture of biotite. d) Detail view of sample BD15, containing garnet, staurolite, biotite, quartz, feldspars, with andalusite apparently growing over the S_2 foliation (post-tectonic porphyroblast growth).

NO COLOR IN PRESS

Thermodynamic Modelling

BD16c

The thermodynamic modelling results for sample BD16c are presented in Fig. 9. Compositional isopleths corresponding to the composition observed in the core of the garnet porphyroblasts indicate the beginning of their growth at ca. 490–500 ºC and 2.5–3.3 kbar (Fig. 10a). Peak metamorphic conditions were constrained in a pseudosection calculated with an effective bulk composition. This composition was obtained using the bulk composition of the sample modified by stepwise fractionation of garnet along a predefined P–T path with the start point of 490 ºC and 3.8 kbar and the endpoint of 510 ºC and 5.0 kbar. The starting point corresponds to the centre of the P–T interval constrained for the garnet core composition, whereas the endpoint was set according to preliminary P–T estimate from garnet rim and matrix minerals isopleths in the pseudosection calculated with the bulk composition. In the pseudosection calculated with the effective bulk composition, garnet rim and muscovite isopleths delimited peak metamorphic conditions of ca. 500–510 ºC and 5–6.4 kbar (Fig. 9b). Modelled composition of biotite shows X_{Mg} = 0.25–26, whereas the observed composition ranges between X_{Mg} = 0.35–0.40. This discrepancy is attributed either to local variations in the chemistry of the sample or to inaccurate formulation of the biotite mixing model.

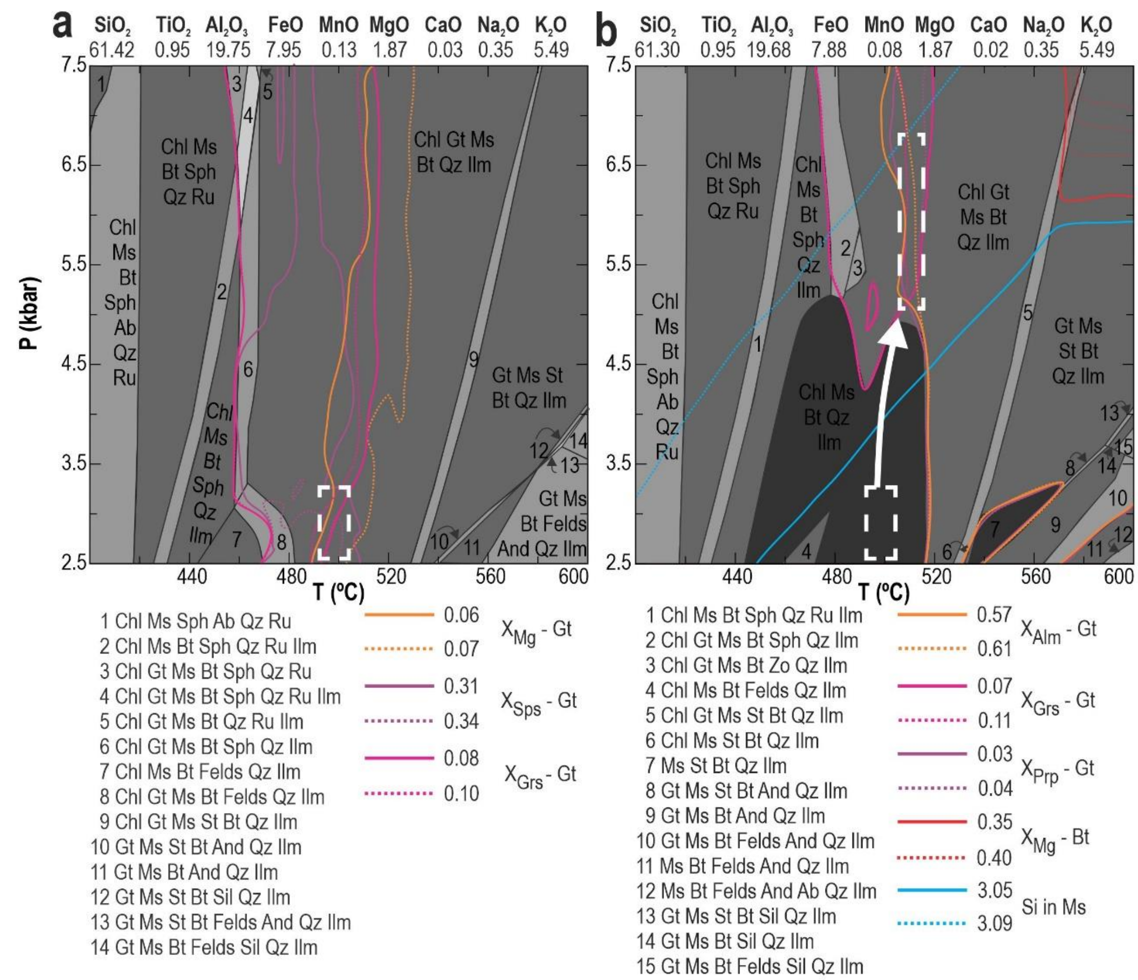

Fig. 9. Thermodynamic modelling results for sample BD16c. a) Pseudosection calculated with whole-rock geochemistry and garnet isopleths. White dashed rectangle indicates conditions for the beginning of garnet growth. b) Pseudosection calculated with composition obtained after the fractionation of garnet and rim garnet and mica isopleths. The second white dashed rectangle indicates peak metamorphic conditions. Arrows indicate a likely metamorphic path from the beginning of garnet growth to peak metamorphic conditions.

NO COLOR IN PRESS

BD-15

P–T pseudosections for sample BD15 are presented in Fig. 10a. Compositional isopleths corresponding to the composition observed in the core of the garnet porphyroblasts constrain the beginning of their growth at ca. 530–550 ºC and 3–4.3 kbar (Fig. 10a). Peak metamorphic conditions were constrained in a pseudosection calculated with an effective bulk composition. This composition was obtained using the bulk composition of the sample modified by stepwise fractionation of garnet along a predefined P–T path with the start point of 540 ºC and 3.6 kbar, corresponding to the beginning of garnet growth, and the endpoint of 630 ºC and 6.5 kbar, corresponding to the centre of the P–T interval constrained by plotting garnet rim and matrix minerals isopleths in the pseudosection calculated with the bulk composition. The pseudosection calculated with the effective bulk composition together with garnet rim and other matrix minerals isopleths show peak metamorphic conditions of ca. 560–570 ºC and 5–5.5 kbar (Fig. 10b).

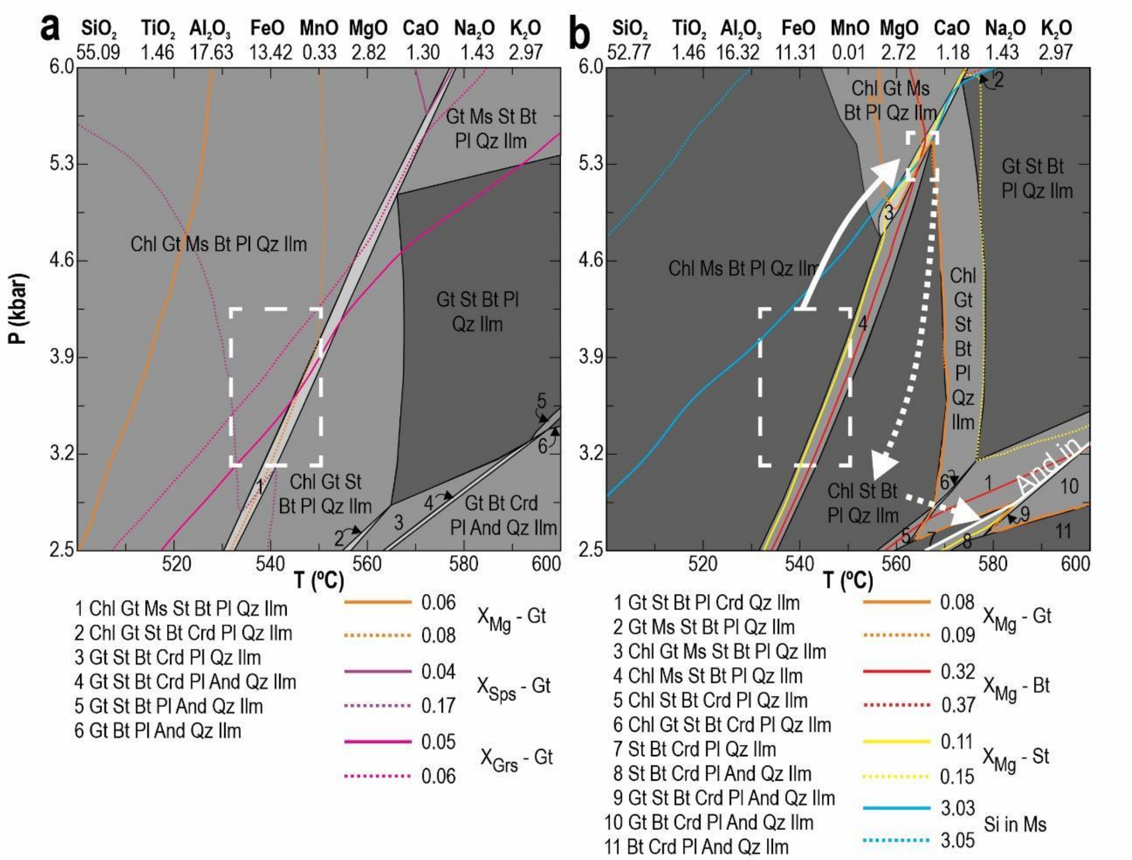

Fig. 10. Thermodynamic modelling results for sample BD15. a) Pseudosection calculated with whole-rock geochemistry and garnet isopleths. White dashed rectangle indicates conditions for the beginning of garnet growth. b) Pseudosection calculated with composition obtained after the fractionation of garnet, garnet rim and mica isopleths. The only isopleth displayed for garnet rim is X_{Mg} since other end-member isopleths look alike. The second white dashed rectangle indicates peak metamorphic conditions. Arrows indicate a likely metamorphic path from the beginning of garnet growth to peak, then exhumation, and, finally, contact metamorphism.

NO COLOR IN PRESS

Discussion

P-T-D path of the Passo Feio Complex

Unlike previous suggestions (e.g. Bitencourt, 1983a), our data lead to the interpretation that M_1 is coeval with D_1–D_2. Bitencourt (1983a) described that M_1 was mainly registered in the garnet and staurolite porphyroblasts and associated with S_1 (D_1), while the matrix and the main foliation recrystallised under biotite-zone conditions during M_2–D_2 retrogression. This author also concluded that D_1 and D_2 were progressive, which is in agreement with our petrographical observations such as rotated garnet or folded inclusion trails of S_1 in which S_2 forms parallel with the axial planes (Fig. 6a-c). In this sense, relict foliation preserved in garnet and staurolite cores (S_1) can be interpreted as an early structure formed at the conditions registered in garnet cores. At the same time, the progression of this deformation phase also formed S_2 at conditions close to those registered in garnet rims. Mineral chemistry data show increasing values of X_{Alm} (Supplementary Table 1) from core to rim, indicating progressive metamorphism during garnet growth. The intersection of isopleths with the composition of porphyroblasts (garnet rim and staurolite) and matrix minerals indicate that M_1 mineral assemblage in pelitic schists is composed of St–Gt–Bt–Ms–Chl–Pl–Qz–Ilm (Fig. 10b). Therefore, andalusite, which was observed in the thin section, is excluded from the paragenesis. Thus, D_1–D_2–M_1 corresponds to a single metamorphic-deformation event.

The P–T conditions registered in the Gt phyllite do not corroborate the interpretation that phyllites in the complex went through a “phyllitization” process, as interpreted by Bitencourt (1983a). As shown in figure 9, conditions for the onset of garnet growth in sample BD16c were ca. 490–500 ºC and 2.5–3.3 kbar, and peak conditions for M_1 were ca. 500–510 ºC and 5–6.4 kbar. We found no register of higher metamorphic conditions, as those constrained for the Gt–St schist. Thus, the disposition of phyllites to the northern and southwestern part of the complex is likely related to the geometry of its regional, double-plunging antiformal structure.

Our results do not support the low-pressure character of M_1 based on the presence of andalusite. This mineral is only found locally, and its crystals typically overgrow the foliation indicating post-S_2 porphyroblast growth (Fig. 8d). Thermodynamic modelling of sample BD15 (Fig. 10), which contains andalusite, determined conditions of ca. 530–550 ºC and 3-4.3 kbar for the beginning of garnet growth, and ca. 560–570 ºC and 5–5.5 kbar for the peak of M_1. The path from the onset of garnet growth to the peak conditions does not intersect the field of andalusite stability. Therefore, andalusite is likely a mineral associated with re-heating of the complex due to the intrusion of the Caçapava Granite at 562 ± 8 Ma (U–Pb on zircon - Remus et al., 2000 – Fig. 11a). This interpretation is corroborated by the fact that andalusite growth is localised, which could be linked to a heterogeneous distribution of heat from the granite body into the sub-horizontal host rocks. The crystallisation of andalusite also implies that the PFC was at a maximum depth of about 14 km during the intrusion (Fig. 11b), as inferred from the maximum pressure conditions for andalusite stability (assuming 3.5 km/kbar – inferred path of Fig. 10b and 11a).

Our results show that D_3 was an important deformation phase mainly localised in the eastern part of the study area (Fig. 3a). In this zone, areas of sub-horizontal foliation, S_2, are found next to areas of dominantly sub-vertical foliation S_3 (Fig. 5). Relicts of S_2 are found between planes of S_3 as F_2 displaced hinges (Fig. 4c), or as cm-size pods (Fig. 4d). Moreover, mylonitic textures (Fig. 7c-e) along subvertical planes, and the subhorizontal NE–SW trending stretching lineation (L_3) corroborate the interpretation of D_3 as the result of a transcurrent movement. Kinematic indicators found at both mesoscopic (Fig. 4e-f) and microscopic scale (Fig. 6c-e), indicate a dextral sense of shear along this shear zone.

Two main observations help to constrain the metamorphic conditions of D_3 structures: (i) biotite crystals aligned in S_3 are finer-grained (Fig. 7) as compared to those found along S_2 (Fig. 6), interpreted to indicate biotite recrystallisation under lower temperature conditions (biotite zone); (ii) two different textural generations of garnet found in the same sample (Fig. 7c-d) may indicate that at least locally, D_3 has reached garnet-zone temperature conditions. In this sample, broken garnet porphyroblasts (Gt_1) are probably associated with M_1. In contrast, much smaller, well-preserved garnet crystals dispersed in the matrix (Gt_2) have grown either before or during the formation of S_3 since the foliation wraps around them. In either case, a more comprehensive dataset is necessary to understand the meaning of Gt_2 since it could also be a late phase of Gt crystallisation simultaneous to the growth of Gt_1 rims.

In order to adequately place the PFC in a broader structural and geological framework, the significance of D_3 structures is analysed together with regional structural data and the previously studied relationship between the PFC and the emplacement of the Caçapava Granite (Nardi & Bitencourt, 1989; Costa et al., 1995). Structural data related to D_3 (S_3 and L_3) and the subhorizontal magmatic lineation reported for the Caçapava Granite (Nardi & Bitencourt, 1989) both indicate the occurrence of shear movements in the region. In fact, previous works have called upon the existence of a dextral shear zone to explain the syntectonic emplacement of the granite (Costa et al., 1995). Furthermore, if one considers the emplacement of the Caçapava Granite to be synchronous with the last deformational phase registered in the PFC, as admitted by previous authors (e.g. Nardi & Bitencourt, 1989; Costa et al., 1995), then the P–T conditions of D_3 – M_2 may be constrained not only by the crystallisation of andalusite due to syn-D_3 contact metamorphism but also by biotite and garnet recrystallised during the development of the D_3 structures (Fig. 11a). Moreover, the relation of PFC M_2–D_3 with the intrusion of the Caçapava Granite places this event at around 562 ± 8 Ma (U-Pb SHRIMP in zircon – Remus et al., 2000 – Fig. 11a, c).

Our results and interpretation of M_2–D_3 provide geological/structural meaning for the 5 km-wide, NE-trending Caçapava Lineament (Fig. 2a). Since we have observed that D_3 structures are most expressive within the area where the CL crosscuts the PFC, featuring mylonitic foliation and stretching lineation, the CL may be defined as related to a dextral transcurrent shear zone affecting the PFC, and thus it may be correctly named as Caçapava Shear Zone (CSZ).

As shown by 3D modelling in Costa et al. (1995), the larger thickness of the granite body, interpreted to be its root, is found in its northwestern part. This would then be the place where the main intrusion conduit would likely be located. Furthermore, as shown in figure 2a, in the northwestern region, there is a structure with a magnetometric signal similar to that observed in the main eastern zone, which we interpret as a branch of the CSZ. Thus, as first suggested by Costa et al. (1995), our data validate the interpretation that a curved branch of the NE-striking, dextral CSZ jogs from ENE-striking extensional domains into NS-striking contractional ones during emplacement of the granitic body (Fig. 11b).

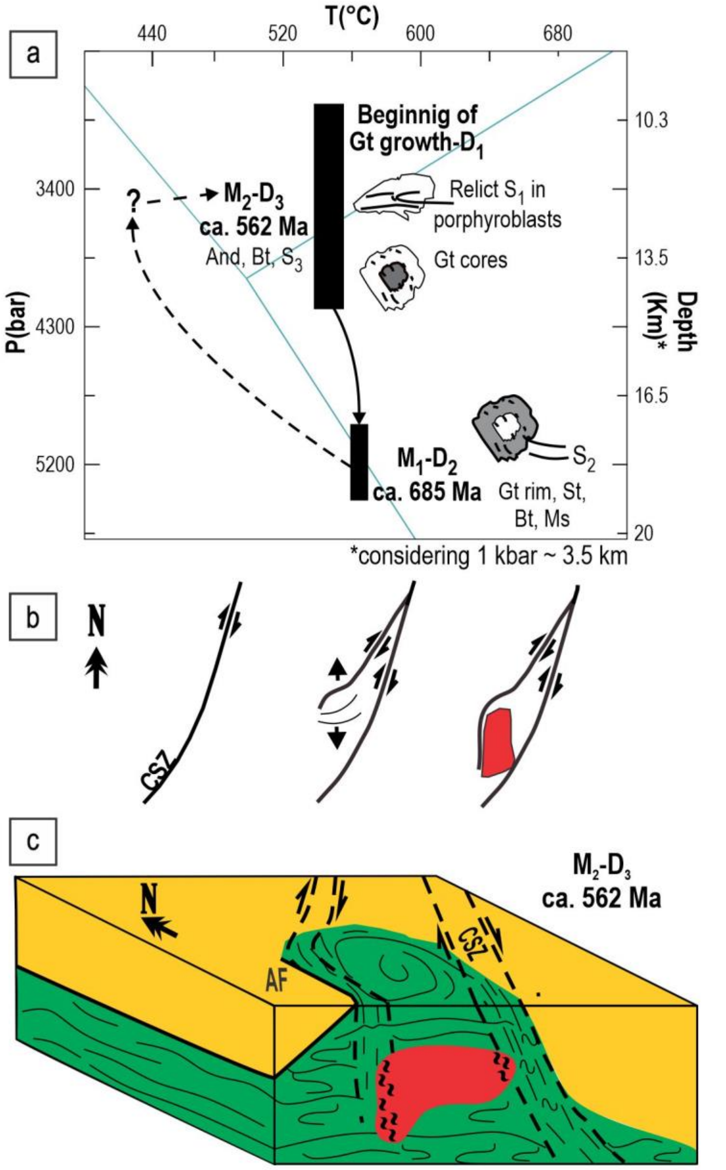

Fig. 11 a) P-T-D path as registered in the metapelitic schists of the Passo Feio Complex, with parageneses associated with each metamorphic event. **b)** Sketch showing the evolution of the Caçapava Shear Zone; from left to right: first, the position of the CSZ, then the development of a branch whose curvature opened space to the intrusion of the granite and, lastly, the final setting of the region. **c)** Sketch of the final scenario of the PFC M_2-D_3 after the intrusion of the Caçapava Granite controlled by the Caçapava Shear Zone.

NO COLOR IN PRESS

Regional Implications

Defining the Caçapava Shear Zone as a structure related to the PFC places additional parameters to discuss the geotectonic history of the Dom Feliciano Belt. Firstly, as Costa (1997) modelled, the structure’s geometry in depth shows that it dips steeply towards E. This is the same dip direction as the Dorsal de Canguçu Shear Zone, the structure that limits the Tijucas Fold Belt and the Pelotas Batholith. Moreover, NE-vergence is typical in the Tijucas Fold Belt, while structures of the São Gabriel Block are described as a SE-directed thrust-stack (Saalmann et al. 2006). Therefore, the in-depth geometry of structures in the Tijucas Fold Belt appears to be more compatible with the development of a shear zone that dips to the E rather than with those of the São Gabriel Block, where the PFC is usually placed.

The kinematics of the CSZ is another point of discussion. Oyhantçabal et al. (2018) suggested a connection between the CSZ and the Sierra de Sosa Shear Zone in Uruguay. However, in contrast with the CSZ, the Sierra de Sosa Shear Zone is sinistral (Oriolo et al., 2016). As mentioned before, previous works have shown sinistral shear sense for the CSZ in their maps (e.g. Philipp et al. 2013, 2018) but no structural data are given to justify it. We assume this inferred kinematic of the CSZ was either based on the prolongation of the Sierra de Sosa to the CSZ or related to previous works in brittle structures of the Camaquã Basin, such as illustrated by Almeida et al. (2012), in which sinistral faults described in the same area are oriented parallel to the CSZ. The constraint we have for the activity of the CSZ is linked to the emplacement of the Caçapava Granite at ca. 562Ma, at midcrustal conditions, and therefore cannot be compared to brittle structures of the Camaqua Basin. However, the further development of the basin has placed these units side by side, and it is likely that the faults parallel to the CSZ to the east of Caçapava do Sul are associated with a sinistral reactivation of the structure, placed by Almeida et al. (2012) near the Ediacaran-Cambrian limit.

More data are still needed to adequately compare the metamorphic path registered in the PFC with those of other metamorphic complexes in south Brazil. The M_1 conditions of ca. 560–570 ºC and 5–5.5 kbar is comparable to the Porongos Metamorphic Complex (Tijucas Fold Belt) peak condition intervals of ca. 560-590ºC and 5.8–6.3 kbar (Lenz, 2006; De Toni et al., 2021) and to the peak conditions of ca. 580 ºC and 6 kbar of a Gt-St schist from the São Gabriel Block (Cerva-Alves et al., 2019). Thus, geothermal gradients of 25–30 ºC/km are observed in both the São Gabriel Block and Tijucas Fold Belt. We point out that a precise geochronological constraint of the PFC first metamorphic event (M_1) will likely confirm the correct tectonic domain of the complex, since the ages of metamorphism are very different in the Sao Gabriel Block (724 ± 28 Ma – post-peak crystallisation of monazite – Cerva-Alves et al., 2019 – in situ U-Th-Pb EPMA), and the Tijucas Fold Belt (658 ± 26 Ma – Rb-Sr isochron muscovite – whole-rock composite of 5 samples – Lenz, 2006).

The block-limiting character of the CSZ is also questioned by the PFC provenance age patterns. The complex had an important contribution from Paleoproterozoic (main peak at 2.0 – 2.2) and Mesoproterozoic (older than 1.0 Ga) sources. Neoproterozoic ages reported are 948 to 803 Ma (Lopes et al., 2015), 810–750 Ma (called Bossoroca Complex – Philipp et al. 2021), and 780–730 Ma and 610–580 Ma (Souza, 2020). On the other hand, the São Gabriel Block has Neooproterozoic provenance ages ranging between 900 and 660 Ma (Philipp et al. 2021; Vedana et al., 2017; Lena et al., 2014), and Archean to Paleoproterozoic provenance ages of 3.6–1.62 Ga (Philipp et al. 2021). Therefore, Paleoproterozoic and Neoproterozoic provenance ages of the São Gabriel Block and PFC overlap to some extent, but Mesoproterozoic and Ediacaran zircon grains are exclusively found in the PFC. Similar Mesoproterozoic ages are reported for the Porongos Metamorphic Complex (Gruber et al., 2016; Hofig et al., 2018; Pertille et al., 2015) and the northern units of the Tijucas Fold Belt (Percival et al., 2021), while Cryogenian–Ediacaran ages associated to the deposition in synorogenic basins were spotted in the Tijucas Fold Belt metasedimentary rocks (Pertille et al. 2017). Thus, based on the available provenance datasets, the PFC more easily compares to the Tijucas Fold Belt, which debunks the CSZ as a block-limiting structure and implies that the limit between the Sao Gabriel Block and Tijucas Fold Belt must be to the west of the PFC, as suggested by Souza (2020).

Conclusions

Our study of the Passo Feio Complex offers the following conclusions regarding its metamorphic-deformation history, relevant to understanding the structural framework of the Dom Feliciano Belt.

I. The first two deformational events, D_1 and D_2, are progressive and coeval to the growth of garnet up to the peak metamorphic conditions found in the complex (M_1).

II. A Gt phyllite sample records conditions for the beginning of garnet growth at ca. 490–500 ºC and 2.5–3.3 kbar and peak metamorphism at ca. 500–510 ºC and 5–6.4 kbar. A Gt–St schist sample indicates the onset of garnet growth at ca. 530–550 ºC and 3–4.3 kbar and peak metamorphic conditions of M_1 at ca. 560–570 ºC and 5–5.5 kbar.

III. After M_1, during which the rocks reached a depth of ca. 17–19 km, the complex was exhumed to a depth of about 14 km or less (~4 kbar), the maximum depth to allow the crystallisation of andalusite due to the effect of contact metamorphism caused by the Caçapava Granite during M_2-D_3. Regions where S_3 is well-developed show the recrystallisation of biotite and relict minerals of M_1, which indicate that M_2 reached intermediate greenschist facies (biotite zone) with pressures not higher than *ca.* 4 kbar (maximum pressure of andalusite).

IV. The similarities of S_3 and L_3 structures of the Passo Feio Complex with the magmatic structures in the Caçapava Granite, together with the orientation of geophysical anomalies in the region, and the observed kinematics of S_3 support the interpretation of the Caçapava Lineament as a probable expression of a dextral shear zone.

V. A curved ENE to NS branch of the NE-striking Caçapava Shear Zone, together with its dextral shear sense, is interpreted to be responsible for accommodating the granite emplacement at ca. 562 Ma and the continued shearing within the same stress field resulting in mylonitic foliation and stretching lineations mainly at its eastern and western borders.

Acknowledgements

We thank the Brazilian Research Council (CNPq) for the MSc scholarship (EOC - 131502/2019-0) and Productivity Grant (MFB – 311501/2019-2), and the Norwegian Agency for International Cooperation and Quality Enhancement in Higher Education (Diku - grant project no. UTF-2018-CAPES-Diku-10004). We are much obliged to Matheus Ariel Battisti, Giuseppe Betino De Toni, Stephanie Carvalho da Silva and Franciele Gonçalves Andres for their help during fieldwork, and Karina Monsen and Muriel Erambert for the help during laboratory and microprobe sessions, respectively. The Regional Editor of JSAES, Monica Heilbron, and reviewers, M. Francisco Pereira and an anonymous reviewer, are acknowledged.

References

Almeida, R. P., Janikian, L., Fragoso-Cesar, A. R. S., & Fambrini, G. L. 2010. The Ediacaran to Cambrian rift system of Southeastern South America: tectonic implications. The Journal of Geology, 118(2):145-161.

Almeida, R. P., Santos, M. G., Fragoso-Cesar, A. R., Janikian, L., & Fambrini, G. L. 2012. Recurring extensional and strike-slip tectonics after the Neoproterozoic collisional events in the southern Mantiqueira province. Anais da Academia Brasileira de Ciências, 84(2):347-376.

Almeida, R.P., Santos, M.G., Fragoso-Cesar, A.R., Janikian, L. and Fambrini, G.L., 2012. Recurring extensional and strike-slip tectonics after the Neoproterozoic collisional events in the southern Mantiqueira province. *Anais da Academia Brasileira de Ciências*, *84*(2), pp.347-376.

Arena, K.R., Hartmann, L.A. & Lana, C. 2016. Evolution of Neoproterozoic ophiolites from the southern Brasiliano Orogen revealed by zircon U–Pb–Hf isotopes and geochemistry. Precambrian Research, 285:299–314.

Babinski, M., Chemale Jr, F., Hartmann, L.A., Van Schmus, W.R. & Silva, C.L., 1996. Juvenile accretion at 750–700 Ma in southern Brazil. Geology, 24(5):439-442.

Basei, M.A., Peel, E., Bettucci, L.S., Preciozzi, F. & Nutman, A.P. 2011. The basement of the Punta del Este Terrane (Uruguay): an African Mesoproterozoic fragment at the eastern border of the South American Río de La Plata craton. International Journal of Earth Sciences, 100(2-3):289-304.

Battisti, M.A.B., Bitencourt, M.F., De Toni, G.B., Nardi, L.V.S. & Konopásek, J. 2018. Metavolcanic rocks and orthogneisses from Porongos and Várzea do Capivarita complexes: A case for identification of tectonic interleaving at different crustal levels from structural and geochemical data in southernmost Brazil. Journal of South American Earth Sciences, 88:253-274.

Bicalho, V, Remus, M.V.D., Rizzardo, R. & Dani, N. 2019. Geochemistry, metamorphic evolution and tectonic significance of metabasites from Caçapava do Sul, southern Brazil. Brazilian Journal of Geology, 49(2).

Bilham, R., Blume, F., Bendick, R. and Gaur, V.K. 1998. Geodetic constraints on the translation and deformation of India: Implications for future great Himalayan earthquakes. Current Science, pp.213-229.

Bitencourt, M.F. & Hartmann, L.A. 1984a. Geoquímica das Rochas Anfibolíticas da Região de Caçapava do Sul, RS – Parte I: Caracterização Geológica e Petrográfica, Elementos Maiores e Menores. In: Anais do XXXIII Congresso Brasileiro de Geologia, Rio de Janeiro, p. 4266-4278.

Bitencourt, M.F. & Hartmann, L.A. 1984b. Geoquímica das Rochas Anfibolíticas da Região de Caçapava do Sul, RS – Parte II: Elementos Traço e Considerações Genéticas. In: Anais do XXXIII Congresso Brasileiro de Geologia, Rio de Janeiro, p. 4253-4265.

Bitencourt, M.F. & Nardi, L.V.S. 2000. Tectonic setting and sources of magmatism related to the Southern Brazilian Shear Belt. Revista Brasileira de Geociências, 30:186–189.

Bitencourt, M.F. 1983a. Metamorfitos da região de Caçapava do Sul, RS – Geologia e Relações com o Corpo Granítico. In: Atas do 1º Simpósio Sul-Brasileiro de Geologia, Porto Alegre, p. 37-48.

Bitencourt, M.F. Geologia, Petrologia e Estrutura dos Metamorfitos da Região de Caçapava do Sul, RS. 1983b. Porto Alegre, 161p. Master Thesis, Programa de Pós-graduação em Geociências, Instituto de Geociências, Universidade Federal do Rio Grande do Sul, Porto Alegre, Brazil.

Bitencourt, M.F., De Toni, G.B., Florisbal, L.M., Nardi, L.V.S., Martil, M.M.D., Heaman, L., DuFrane, A., Chemale Jr., F., 2016. Timing of syenitic syntectonic magmatism as a record of strain partitioning during Cryogenian collisional transpressive regime in southernmost Brazil. in: Primer Simposio de Tectonica Sudamericana – Acta. Santiago, Chile. 206 p.

Borba, A. W., Vignol-Lelarge, M.L.M., Mizusaki, A.M.P. 2002. Uplift and denudation of the Caçapava do Sul granitoids (southern Brazil) during Late Paleozoic and Mesozoic: constraints from apatite fission-track data. Journal of South American Earth Sciences, 15(6):683-692.

Cerva-Alves, T., Hartmann, L.A., Queiroga, G.N., Remus, M.V.D. 2019. Evolution of Tonian Metamorphic Events in the Cambaizinho Ophiolite, São Gabriel Terrane. In: Anais do XI international Symposium on Tectonics, Bento Gonçalves, Brasil.

Chemale Jr., F. 2000. Evolução Geológica do Escudo Sul-rio-grandense. In: Geologia do Rio Grande do Sul. CIGO/UFRGS, Porto Alegre, 2002. 444 p.

Connolly, J.A.D. 2005. Computation of phase equilibria by linear programming: a tool for geodynamic modeling and its application to subduction zone decarbonation. Earth and Planetary Science Letters, 236(1-2):524-41.

Connolly, J.A.D. 2009. The geodynamic equation of state: what and how. Geochemistry, Geophysics, Geosystems, 10(10).

Costa, A.F.U. 1997. Teste e modelagem geofísica da estruturação das associações litotectônicas pré-cambrianas no escudo sul-rio-grandense. Porto Alegre, 180p. PhD Thesis, Instituto de Geociências, Universidade Federal do Rio Grande do Sul, Porto Alegre, Brazil.

Costa, A.F.U., Fernandes, L.A.D., Shukowsky, W., Nardi, L.V.S., & Bitencourt, M.F. 1995. Teste dos modelos tectônicos e de posicionamento do Complexo Granítico de Caçapava do Sul através de estudos de modelagem gravimétrica 3-D. *Revista Brasileira de Geofísica*, *13*(2):91-101.

CPRM - Serviço Geológico do Brasil. 2010. Projeto Aerogeofísico Escudo do Rio Grande do Sul. LASA PROSPECÇÕES S.A., Relatório Técnico, 260 p.

De Toni, G.B., Bitencourt, M.F., Konopásek, J., Battisti, M.A., Costa, E.O., & Savian, J.F. 2021. Autochtonous origin of the Encruzilhada Block, Dom Feliciano Belt, southern Brazil, based on aerogeophysics, image analysis and PT-paths. *Journal of Geodynamics*, 101825.

De Toni, G.B., Bitencourt, M.F., Nardi, L.V.S, Florisbal, L.M., Almeida, B.S. & Geraldes, M., 2020a. Dom Feliciano Belt orogenic cycle tracked by its pre-collisional magmatism: the Tonian (ca. 800 Ma) Porto Belo Complex and its correlations in southern Brazil and Uruguay. Precambrian Research, 342, 105702.

Fernandes, L.A.D., Menegat, R., Costa, A.F.U., Koester, E., Kramer, G., Tommasi, A., Porcher, C.C., Ramgrab, G.E. & Camozzato, E. 1995a. Evolução tectônica do Cinturão Dom Feliciano no Escudo Sul-rio-grandense: Parte I -uma contribuição a partir do registro geológico. Revista Brasileira Geociências, 25:351-374.

Fernandes, L.A.D., Menegat, R., Costa, A.F.U., Koester, E., Kramer, G., Tommasi, A., Porcher, C.C., Ramgrab, G.E. & Camozzato, E. 1995b. Evolução tectônica do Cinturão Dom Feliciano no Escudo Sul-rio-grandense: Parte II –uma contribuição a partir das assinaturas geofísicas. Revista Brasileira Geociências, 25:375-384.

Fuhrman, M.L. & Lindsley, D.H. 1988. Ternary-feldspar modeling and thermometry. American mineralogist, 73(3-4):201-215.

Gansser, A. 1964. The Geology of the Himalayas. Wiley Interscience, New York, 289 pp.

Gruber, L., Porcher, C.C., Koester, E., Bertotti, A.L., Lenz, C.,Fernandes, L.A.D. & Remus, M.V.D. 2016. Isotope Geochemistry and Geochronology of Syn-Depositional Volcanism in Porongos Metamorphic Complex, Santana Da Boa Vista Antiform, Dom

Feliciano Belt, Brazil: Onset of an 800 Ma Continental Arc. Journal of Sedimentary Environments, 1(2):202-221.

Gubert, M.L., Philipp, R.P. & Basei, M.A.S. 2016. The Bossoroca Complex, São Gabriel Terrane, Dom Feliciano Belt, southernmost Brazil: U-Pb geochronology and tectonic implications for the neoproterozoic São Gabriel Arc. Journal of South American Earth Sciences, 70:1-17.

Hartmann, L.A., Lopes, W.R. & Savian, J.,F. 2016. Integrated evaluation of the geology, aerogammaspectrometry and aeromagnetometry of the Sul-Riograndense Shield, southernmost Brazil. Anais da Academia Brasileira de Ciências, 188(1):75-92.

Hartmann, L.A., Philipp, R.P., Santos, J.O.S. & McNaughton, N.J. 2011. Time frame of 753–680 Ma juvenile accretion during the São Gabriel orogeny, southern Brazilian Shield. Gondwana Research, 19(1):84-99.

Hartmann, L.A., Tindle, A. & Bitencourt, M.F. 1990. O metamorfismo de fácies anfibolito no Complexo Metamórfico Passo Feio, RS, com base em química dos minerais. Pesquisas em Geociências, 17(1-2):62-71.

Hasui, Y., Carneiro, C.D.R. & Coimbra, A.M. 1975. The Ribeira Fold Belt. Revista Brasileira de Geociências, 5(4):257-266.

Höfig, D.F., Marques, J.C., Basei, M.A.S., Giusti, R.O., Kohlrausch, C. & Frantz, J.C. 2017. Detrital zircon geochronology (U-Pb LA-ICP-MS) of syn-orogenic basins in SW Gondwana: new insights into the cryogenian-ediacaran of Porongos complex, Dom Feliciano belt, southern Brazil. Precambrian Research, 306:189-208.

Höfig, D.F., Marques, J.C., Basei, M.A.S., Giusti, R.O., Kohlrausch, C. and Frantz, J.C., 2018. Detrital zircon geochronology (U-Pb LA-ICP-MS) of syn-orogenic basins in SW Gondwana: New insights into the Cryogenian-Ediacaran of Porongos Complex, Dom Feliciano Belt, southern Brazil. Precambrian Research, 306:189-208.

Holland, T.J.B.JB & Powell, R.T.J.B.TJB 1998. An internally consistent thermodynamic data set for phases of petrological interest. Journal of metamorphic Geology, 16(3):309-343.

Jost, H. & Bitencourt, M.F. 1980. Estratigrafia e tectônica de uma fração da Faixa de Dobramentos Tijucas no Rio Grande do Sul. Acta Geológica Leopoldensia, 4(7):27-60.

Jost, H. & Hartmann, L.A.. 1984. Província Mantiqueira – Setor Meridional. In: Pré-Cambriano do Brasil. Coord.: Almeida, F.F.M., Hasui, Y., p. 345-368.

Koester, E., Porcher, C.C., Pimentel, M.M., Fernandes, L.A.D., Vignol-Lelarge, M.L., Oliveira, L.D. & Ramos, R.C., 2016. Further evidence of 777 Ma subduction-related continental arc magmatism in Eastern Dom Feliciano Belt, southern Brazil: the Chácara das Pedras Orthogneiss. Journal of South American Earth Sciences, 68:155-166.

Konopásek, J., Cavalcante, C., Fossen, H. & Janoušek, V., 2020. Adamastor – an ocean that never existed? Earth-Science Reviews 205, p.103201.

Konopásek, J., Janoušek, V., Oyhantçabal, P., Sláma J. & Ulrich, S. 2018. Did the circum-Rodinia subduction trigger the Neoproterozoic rifting along the Congo–Kalahari Craton margin? International Journal of Earth Sciences, 107(5):1859-1894.

Leite, J.A., Hartman, L.A., Mcnaughton, N.J. & Chemale Jr, F. 1998. SHRIMP U/Pb zircon geochronology of Neoproterozoic juvenile and crustal-reworked terranes in southernmost Brazil. International Geology Review, 40(8):688-705.

Lena, L.O.F., Pimentel, M.M., Philipp, R.P., Armstrong, R. & Sato, K. 2014. The evolution of the Neoproterozoic São Gabriel juvenile terrane, southern Brazil based on high spatial resolution U-Pb ages and δ18O data from detrital zircons. Precambrian Research, 247:126-138.

Lenz, C. 2006. Evolução metamórfica dos metapelitos da Antiforme Serra Dos Pedrosas: condições e idades do metamorfismo. Porto Alegre, 128 p. Master's Thesis, Programa de Pós-graduação em Geociências, Instituto de Geociências, Universidade Federal do Rio Grande do Sul, Porto Alegre, Brazil.

Lenz, C., Fernandes, L.A.D., McNaughton, N.J., Porcher, C.C. & Masquelin, H. 2011. U–Pb SHRIMP ages for the Cerro Bori orthogneisses, Dom Feliciano Belt in Uruguay: evidences of a ~ 800 Ma magmatic and ~ 650 Ma metamorphic event. Precambrian Research, 185:149–163

Lenz, C., Porcher, C.C., Fernandes, L.A.D., Masquelin, H., Koester, E. & Conceição, R.V. 2013. Geochemistry of the Neoproterozoic (800–767 Ma) Cerro Bori orthogneisses, Dom Feliciano Belt in Uruguay: tectonic evolution of an ancient continental arc. Mineralogy and Petrology, 107:785 – 806.

Lopes, C.G., Pimentel, M.M., Philipp, R.P., Gruber, L., Armstrong, R. & Junges, S. 2015. Provenance of the Passo Feio Complex, Dom Feliciano Belt: implications for the age of supracrustal rocks of the São Gabriel Arc, southern Brazil. Journal of South American Earth Sciences, 58:9-17.

Machado, N., Koppe, J.C. & Hartmann, L.A., 1990. A late Proterozoic U-Pb age for the Bossoroca Belt, Rio Grande do Sul, Brazil. Journal of South American Earth Sciences, 3(2-3):87-90.

Martil, M.M.D., Bitencourt, M.F., Nardi, L.V.S., Koester, E. & Pimentel, M.M. 2017. Pre-collisional, Neoproterozoic (ca. 790 Ma) continental arc magmatism in southern Mantiqueira Province, Brazil: geochemical and isotopic constraints from the Várzea do Capivarita Complex. Lithos, 274–275:39–52.

Masquelin H., Fernandes, L.A.D., Lenz, C., Porcher, C.C. & McNaughton, N.J. 2012. The Cerro Olivo Complex: a pre-collisional Neoproterozoic magmatic arc in Eastern Uruguay. International Geology Review, 54:1161–1183.

Nakata, T.. 1989. Active faults of the Himalaya of India and Nepal. Tectonics of the Western Himalayas, 232, pp. 243-264.

Nardi, L.V.S. & Bitencourt, M.F. 1989. Geologia, petrologia e geoquímica do Complexo Granítico de Caçapava do Sul, RS. *Revista Brasileira de Geociências*, *19*(2):153-169.

Nardi, L.V.S., Plá-Cid, J., Bitencourt, M.F. & Stabel, L.Z. 2008. Geochemistry and petrogenesis of post-collisional ultrapotassic syenites and granites from southernmost Brazil: the Piquiri Syenite Massif. Anais da Academia Brasileira de Ciências 80(2): 353-371.

Oriolo S., Oyhantçabal P., Wemmer K. & Siegesmund S. 2017. Contemporaneous assembly of Western Gondwana and final Rodinia break-up: Implications for the supercontinent cycle. Geoscience Frontiers, 8:1431-1445.

Oriolo, S., Oyhantçabal, P., Konopásek, J., Basei, M.A., Frei, R., Sláma, J., Wemmer, K. and Siegesmund, S. 2019. Late Paleoproterozoic and Mesoproterozoic magmatism of the Nico Pérez Terrane (Uruguay): tightening up correlations in southwestern Gondwana. Precambrian Research, 327:296-313.

Oriolo, S., Oyhantçabal, P., Wemmer, K., Heidelbach, F., Pfänder, J., Basei, M.A., Hueck, M., Hannich, F., Sperner, B. and Siegesmund, S., 2016. Shear zone evolution and timing of deformation in the Neoproterozoic transpressional Dom Feliciano Belt, Uruguay. *Journal of Structural Geology*, *92*, pp.59-78.

Oyhantçabal, P., Oriolo, S., Philipp, R.P., Wemmer, K. and Siegesmund, S., 2018. The Nico Pérez Terrane of Uruguay and Southeastern Brazil. In *Geology of Southwest Gondwana* (pp. 161-188). Springer, Cham.

Oyhantçabal, P., Siegesmund, S. & Wemmer, K., 2011. The Río de la Plata Craton: a review of units, boundaries, ages and isotopic signature. International Journal of Earth Sciences, 100:201-220.

Oyhantçabal, P., Siegesmund, S., Wemmer, K., Presnyakov, S. & Layer, P. 2009. Geochronological constraints on the evolution of the southern Dom Feliciano Belt (Uruguay). Journal of the Geological Society of London, 166:1075-1084.

Padilha, D.F., Bitencourt, M.F., Nardi, L.V.S., Forisbal, L.M., Reis, C. Geraldes, M. & Almeida, B.S. 2019. Sources and settings of Ediacaran post-collisional syenite-monzonite-diorite shoshonitic magmatism from southernmost Brazil. Lithos, 344-345, 482-503.

Paim, P.S.G., Chemale Jr., F. & Wildner, W. 2014. Estágios evolutivos da Bacia do Camaquã (RS). Ciência e Natura, Santa Maria, 36:183–193.

Percival, J. J., Konopásek, J., Eiesland, R., Sláma, J., de Campos, R. S., Battisti, M. A., & de Fátima Bitencourt, M. 2021. Pre-orogenic connection of the foreland domains of the Kaoko–Dom Feliciano–Gariep orogenic system. Precambrian Research, 354, 106060.

Pertille J., Hartmann L.A., Philipp R.P., Petry T.S. & Lana C.C. 2015. Origin of the Ediacaran Porongos Group, Dom Feliciano Belt, southern Brazilian Shield, with emphasis on whole rock and detrital zircon geochemistry and U-Pb, Lu-Hf isotopes. Journal of South American Earth Sciences, 64:69-93.

Pertille, J., Hartmann, L. A., Santos, J. O. S., McNaughton, N. J., & Armstrong, R. 2017. Reconstructing the Cryogenian–Ediacaran evolution of the Porongos fold and thrust belt, Southern Brasiliano Orogen, based on Zircon U–Pb–Hf–O isotopes. *International Geology Review*, *59*(12):1532-1560. DOI: 10.1080/00206814.2017.1285257

Pertille, J., Hartmann, L.A., Santos, J.O.S., McNaughton, N.J., & Armstrong, R. 2017. Reconstructing the Cryogenian–Ediacaran evolution of the Porongos fold and thrust belt, Southern Brasiliano Orogen, based on Zircon U–Pb–Hf–O isotopes. *International Geology Review*, *59*(12):1532-1560.

Philipp, R.P., Machado, R., Nardi, L.V.S. & Lafon, J.M. 2002. O Magmatismo Granítico Neoproterozóico do Batólito Pelotas no sul do Brasil: Novos dados e revisão da Geocronologia regional. Brazilian Journal of Geology, 32:277-290.

Philipp, R.P., Massonne, H.J., & Campos, R.S. 2013. Peraluminous leucogranites of the Cordilheira Suite: A record of Neoproterozoic collision and the generation of the Pelotas Batholith, Dom Feliciano Belt, Southern Brazil. *Journal of South American Earth Sciences*, *43*: 8-24.

Philipp, R.P., Pimentel, M.M. & Basei, M.A.S. 2018. The Tectonic Evolution of the São Gabriel Terrane, Dom Feliciano Belt, Southern Brazil: The Closure of the Charrua

Ocean. in: S. Siegesmund et al. (eds.), Geology of Southwest Gondwana, Regional Geology Reviews, p. 243-265.

Philipp, R.P., Pimentel, M.M., & Chemale Jr, F. 2016. Tectonic evolution of the Dom Feliciano Belt in Southern Brazil: geological relationships and U-Pb geochronology. Brazilian Journal of Geology, 46:83-104.

Philipp, R.P., Pimentel, M.M., Basei, M.A.S., Salvi, M., Lena, L.O.F., Vedana, L.A., Gubert, M.L., Lopes, C.G., Laux, J.H. and Camozzato, E., 2021. U–Pb detrital zircon dating applied to metavolcano-sedimentary complexes of the São Gabriel Terrane: New constraints on the evolution of the Dom Feliciano Belt. *Journal of South American Earth Sciences*, p.103409.

Preciozzi F, Masquelin H & Basei MAS. 1999. The namaqua/grenville terrane of eastern Uruguay. 2nd South American symposium on isotope geology, Argentina, pp 338–340.

Ramos, R.C., Koester, E., Triboli, D.V., Porcher, C.C., Gezatt, J.N., Silveira, Chaves, R. R., Edinei, K., Triboli, V. D., Cristine, P. C., Neri, G. J., & Luiz, S. R. 2018. Insights on the evolution of the Arroio Grande Ophiolite (Dom Feliciano Belt, Brazil) from Rb-Sr and SHRIMP U-Pb isotopic geochemistry. Journal of South American Earth Sciences, 86:38-53.

Remus, M.V.D., Hartmann, L.A., McNaughton, N.J., Groves, D.I. & Fletcher, I. R. 2000. The link between hydrothermal epigenetic copper mineralization mineralisation and the Caçapava Granite of the Brasiliano Cycle in southern Brazil. Journal of South American Earth Sciences, 13(3): 191-216.

Remus, M.V.D., McNaughton, N.J., Hartmann, L.A., Koppe, J.C., Fletcher, I.R., Groves, D.I. & Pinto, V.M. 1999. Gold in the Neoproterozoic juvenile Bossoroca Volcanic Arc of southernmost Brazil: isotopic constraints on timing and sources. Journal of South American Earth Sciences, 12(4):349-366.

Rivera, C.B., 2019. Construção do Maciço Sienítico Piquiri (609 a 583 ma) por colocação sucessiva de pulsos de magma ultrapotássico e shoshonítico sob extensão no Escudo Sul-rio-grandense. PhD thesis. Universidade Federal do Rio Grande do Sul. Porto Alegre, Brazil.

Saalmann, K., Gerdes, A., Lahaye, Y., Hartmann, L. A., Remus, M. V. D. & Läufer, A. 2011. Multiple accretion at the eastern margin of the Rio de la Plata craton: the prolonged Brasiliano orogeny in southernmost Brazil. International Journal of Earth Sciences, 100(2-3): 355-378.

Saalmann, K., Remus, M.V.D. & Hartmann, L.A. 2006. Structural evolution and tectonic setting of the Porongos Belt, southern Brazil. Geological Magazine, 143:59-88.

Souza, T.L.D., 2020. Gênese dos serpentinitos e esteatitos do Complexo Passo Feio (RS-Brasil): evidências mineralógicas, geoquímicas e isotópicas. https://www.lume.ufrgs.br/handle/10183/221352 204f.

UFRGS, Universidade Federal do Rio Grande do Sul. 1998. Projeto Caçapava do Sul: mapeamento geológico, 1:25.000.

Vedana, L.A., Philipp, R.P. & Basei, M.A.S. 2018. Tonian to early Cryogenian synorogenic basin of the São Gabriel Terrane, Dom Feliciano Belt, southernmost Brazil. *International Geology Review*, *60*(1):109-133.

White, R.W., Powell, R.O.G.E.R.OGER, Holland, T.J.B., Johnson, T.E. & Green, E.C.R.CR 2014. New mineral activity–composition relations for thermodynamic calculations in metapelitic systems. Journal of Metamorphic Geology, 32(3):261-286.

Wildner, W., Ramgraab, G.E. Lopes, R.C. & Iglesias, C.M.F. 2006. Mapa geológico do Estado do Rio Grande do Sul, escala 1:750.000. CPRM, Porto Alegre.

Will, T.M., Gaucher, C., Ling, X.X., Li, X.H., Li, Q.L. & Frimmel, H.E. 2019. Neoproterozoic magmatic and metamorphic events in the Cuchilla Dionisio Terrane, Uruguay, and possible correlations across the South Atlantic. *Precambrian Research*, *320*:303-322.

Sample BD15

Mineral	Garnet										Staurolite						
Point	35/1.	37/1.	43/1.	44/1.	52/1.	53/1.	54/1.	60/1.	61/1.		39/1.	45/1.	49/1.	51/1.	57/1.	58/1.	62/1.
Position	Core	Rim	Core	Rim	Core	Rim	Core	Rim	Core								
Wt%																	
SiO2	36.52	36.76	36.39	36.61	36.44	36.45	36.15	36.05	36.36		26.96	27.48	27.64	27.56	27.16	26.90	27.23
TiO2	0.05	0.02	0.04	0.02	0.08	0.04	0.06	0.00	0.11		0.36	0.37	0.38	0.43	0.43	0.49	0.38
Cr2O3	0.00	0.02	0.05	0.04	0.01	0.00	0.02	0.04	0.16		0.02	0.03	0.01	0.11	0.03	0.07	0.09
Al2O3	20.65	20.77	20.86	20.61	20.66	20.61	20.48	20.70	20.57		55.14	54.03	53.86	54.10	54.42	55.40	54.80
FeO	35.79	37.19	35.93	37.54	33.25	37.37	37.54	38.49	32.18		13.13	12.81	12.73	13.47	13.55	13.63	13.04
MnO	3.43	1.35	3.55	1.46	5.97	1.55	1.88	1.42	7.60		0.14	0.10	0.10	0.11	0.14	0.12	0.16
MgO	1.55	1.92	1.56	1.87	1.21	1.75	1.72	1.95	1.16		1.12	1.01	1.19	1.30	1.20	1.06	0.88
CaO	1.75	1.48	1.61	1.31	2.05	1.52	1.67	1.13	2.16		0.00	0.00	0.00	0.01	0.01	0.00	0.01
Na2O	0.00	0.03	0.02	0.01	0.01	0.01	0.00	0.03	0.03		0.02	0.04	0.03	0.02	0.01	0.03	0.02
K2O	0.00	0.00	0.00	0.01	0.00	0.01	0.00	0.01	0.01		0.01	0.02	0.02	0.00	0.00	0.01	0.00
ZnO	0.00	0.00	0.00	0.00	0.00	0.00	0.00	0.00	0.00		0.37	0.32	0.25	0.35	0.27	0.42	0.39
Total	99.74	99.54	100.01	99.48	99.68	99.31	99.52	99.82	100.34		97.27	96.21	96.21	97.46	97.22	98.13	97.00
12O										**24O**							
Si	2.98	3.00	2.96	2.99	2.98	2.99	2.96	2.94	2.96		3.84	3.96	3.98	3.93	3.87	3.80	3.89
Ti	0.00	0.00	0.00	0.00	0.01	0.00	0.00	0.00	0.01		0.04	0.04	0.04	0.05	0.05	0.05	0.04
Cr	0.00	0.00	0.00	0.00	0.00	0.00	0.00	0.00	0.01		0.00	0.00	0.00	0.01	0.00	0.01	0.01
Al	1.99	2.00	2.00	1.99	1.99	1.99	1.98	1.99	1.97		9.26	9.18	9.14	9.08	9.15	9.23	9.24
Fe3+	0.04	0.00	0.06	0.02	0.03	0.03	0.09	0.13	0.09		0.00	0.00	0.00	0.00	0.00	0.00	0.00
Fe2+	2.41	2.54	2.38	2.55	2.24	2.53	2.48	2.50	2.10		1.56	1.54	1.53	1.60	1.62	1.61	1.56
Mn	0.24	0.09	0.24	0.10	0.41	0.11	0.13	0.10	0.52		0.02	0.01	0.01	0.01	0.02	0.01	0.02
Mg	0.19	0.23	0.19	0.23	0.15	0.21	0.21	0.24	0.14		0.24	0.22	0.25	0.28	0.26	0.22	0.19
Ca	0.15	0.13	0.14	0.12	0.18	0.13	0.15	0.10	0.19		0.00	0.00	0.00	0.00	0.00	0.00	0.00
Na	0.00	0.00	0.00	0.00	0.00	0.00	0.00	0.00	0.00		0.01	0.01	0.01	0.00	0.00	0.01	0.01
K	0.00	0.00	0.00	0.00	0.00	0.00	0.00	0.00	0.00		0.00	0.00	0.00	0.00	0.00	0.00	0.00
Zn	0.00	0.00	0.00	0.00	0.00	0.00	0.00	0.00	0.00		0.01	0.03	0.03	0.04	0.03	0.04	0.04
Total	8.00	8.00	8.00	8.00	8.00	8.00	8.00	8.00	8.00		15.00	15.00	15.00	15.00	15.00	15.00	15.00
XMg	0.07	0.08	0.07	0.08	0.06	0.08	0.08	0.09	0.06		0.13	0.13	0.14	0.15	0.14	0.12	0.11
XGrs	0.05	0.04	0.05	0.04	0.06	0.04	0.05	0.03	0.06								
XSps	0.08	0.03	0.08	0.03	0.14	0.04	0.04	0.03	0.17								
XAlm	0.81	0.85	0.81	0.85	0.75	0.85	0.84	0.85	0.71								
XPrp	0.06	0.08	0.06	0.08	0.05	0.07	0.07	0.08	0.05								
XAn																	

BD16c																	
Mineral						**Garnet**									**Muscovite**		
Point	1/1.	4/1.	7/1.	8/1.	9/1.	14/1.	15/1.	17/1.	19/1.	20/1.	21/1.		3/1.	5/1.	12/1.	13/1.	18/1.
Position	Core	Rim	Core	Core	Rim	Core	Rim	Rim	Core	Rim	Rim		Matrix	Matrix	Matrix	Matrix	Matrix
Wt%																	
SiO2	34.62	36.67	36.37	36.51	36.43	36.37	36.28	36.45	36.18	36.46	36.00		46.03	45.99	45.22	45.00	46.79
TiO2	0.18	0.11	0.13	0.19	0.13	0.14	0.17	0.11	0.13	0.09	0.14		0.25	0.26	0.28	0.27	0.26
Cr2O3	0.01	0.02	0.01	0.02	0.02	0.04	0.00	0.01	0.02	0.03	0.00		0.02	0.00	0.04	0.00	0.01
Al2O3	20.44	20.72	20.55	20.45	20.49	20.14	20.59	20.49	20.32	20.15	20.67		36.27	36.04	33.38	34.04	33.44
FeO	23.26	25.45	24.57	23.99	26.05	23.89	26.69	26.32	23.05	27.86	27.82		2.11	2.34	3.20	2.60	2.67
MnO	17.13	12.86	14.01	14.63	12.00	14.74	13.07	13.47	15.97	10.31	10.63		0.00	0.02	0.01	0.00	0.07
MgO	0.80	0.90	0.89	0.77	0.86	0.82	0.88	0.89	0.83	1.01	1.05		0.64	0.60	1.01	0.72	0.95
CaO	3.59	3.43	3.39	3.55	4.05	3.00	2.52	2.59	3.42	3.72	3.76		0.00	0.00	0.00	0.00	0.00
Na2O	0.00	0.03	0.01	0.03	0.04	0.08	0.01	0.00	0.02	0.00	0.03		0.88	0.78	0.66	0.72	0.54
K2O	0.00	0.00	0.00	0.00	0.00	0.02	0.00	0.01	0.00	0.02	0.00		9.71	9.87	9.61	9.46	9.79
ZnO	0.00	0.00	0.00	0.00	0.00	0.00	0.00	0.00	0.00	0.00	0.00		0.00	0.00	0.00	0.00	0.00
Total	100.03	100.19	99.93	100.14	100.07	99.24	100.21	100.34	99.94	99.65	100.10		95.91	95.90	93.41	92.81	94.52
12O												**11O**					
Si	2.83	2.98	2.97	2.97	2.96	2.99	2.96	2.97	2.95	2.98	2.93		3.05	3.05	3.09	3.09	3.06
Ti	0.01	0.01	0.01	0.01	0.01	0.01	0.01	0.01	0.01	0.01	0.01		0.01	0.01	0.01	0.01	0.01
Cr	0.00	0.00	0.00	0.00	0.00	0.00	0.00	0.00	0.00	0.00	0.00		0.00	0.00	0.00	0.00	0.00
Al	1.97	1.98	1.98	1.96	1.96	1.95	1.98	1.97	1.95	1.94	1.98		2.83	2.83	2.69	2.75	2.66
Fe3+	0.35	0.05	0.08	0.07	0.10	0.06	0.08	0.08	0.12	0.09	0.15		0.00	0.00	0.03	0.00	0.00
Fe2+	1.24	1.68	1.60	1.56	1.68	1.58	1.74	1.71	1.45	1.82	1.74		0.12	0.13	0.15	0.15	0.15
Mn	1.19	0.88	0.97	1.01	0.83	1.03	0.90	0.93	1.10	0.71	0.73		0.00	0.00	0.00	0.00	0.00
Mg	0.10	0.11	0.11	0.09	0.10	0.10	0.11	0.11	0.10	0.12	0.13		0.06	0.06	0.10	0.07	0.10
Ca	0.31	0.30	0.30	0.31	0.35	0.26	0.22	0.23	0.30	0.33	0.33		0.00	0.00	0.00	0.00	0.00
Na	0.00	0.01	0.00	0.01	0.01	0.01	0.00	0.00	0.00	0.00	0.00		0.11	0.10	0.09	0.10	0.07
K	0.00	0.00	0.00	0.00	0.00	0.00	0.00	0.00	0.00	0.00	0.00		0.82	0.83	0.84	0.83	0.84
Zn	0.00	0.00	0.00	0.00	0.00	0.00	0.00	0.00	0.00	0.00	0.00		0.00	0.00	0.00	0.00	0.00
Total	8.00	8.00	8.00	8.00	8.00	8.00	8.00	8.00	8.00	8.00	8.00		7.00	7.00	7.00	7.00	7.00
XMg	0.07	0.06	0.06	0.05	0.06	0.06	0.06	0.06	0.06	0.06	0.07						
XGrs	0.09	0.10	0.09	0.10	0.11	0.08	0.07	0.07	0.09	0.10	0.10						
XSps	0.32	0.29	0.31	0.32	0.26	0.33	0.19	0.30	0.34	0.23	0.22						
XAlm	0.44	0.57	0.54	0.53	0.57	0.53	0.59	0.57	0.49	0.61	0.59						
XPrp	0.04	0.04	0.04	0.03	0.03	0.03	0.04	0.04	0.03	0.04	0.04						

	Muscovite			Plagioclase		Biotite			Chlorite	Ilmenite	
	42/1.	50/1.	56/1.	48/1.	59/1.	38/1.	46/1.	55/1.	41/1.	36/1.	63/1.
	Matrix	Matrix	Matrix	Matrix	Matrix	Matrix	Matrix	Matrix	Matrix	Matrix	Matrix
	45.01	44.78	45.95	63.63	64.07	34.69	34.06	34.21	23.61	0.02	0.00
	0.27	0.19	0.26	0.01	0.01	1.57	1.60	1.66	0.07	53.36	53.74
	0.03	0.06	0.02	0.01	0.00	0.01	0.05	0.04	0.00	0.00	0.05
	36.84	36.30	37.26	22.28	18.27	20.09	19.41	20.60	22.00	0.00	0.00
	0.79	0.77	0.89	0.11	0.23	21.55	22.74	22.47	28.93	44.93	46.09
	0.01	0.04	0.00	0.03	0.03	0.08	0.05	0.09	0.13	1.39	0.67
	0.26	0.32	0.42	0.01	0.01	7.40	7.22	5.99	11.69	0.08	0.19
	0.02	0.00	0.00	3.80	0.00	0.00	0.00	0.04	0.05	0.00	0.00
	1.41	1.43	1.75	9.87	0.19	0.17	0.07	0.09	0.00	0.00	0.02
	8.96	8.58	8.38	0.07	13.63	8.75	8.92	8.96	0.03	0.00	0.00
	0.00	0.00	0.00	0.00	0.00	0.00	0.00	0.00	0.00	0.00	0.00
	93.60	92.47	94.93	99.82	96.44	94.31	94.12	94.15	86.51	99.78	100.76
11O				**8O**		**11O**			**14O**	**3O**	
	3.03	3.05	3.05	2.81	2.98	2.77	2.74	2.76	2.58	0.00	0.00
	0.01	0.01	0.01	0.00	0.00	0.09	0.10	0.10	0.01	1.02	1.01
	0.00	0.00	0.00	0.00	0.00	0.00	0.00	0.00	0.00	0.00	0.00
	2.93	2.92	2.91	1.16	1.00	1.89	1.84	1.96	2.84	0.00	0.00
	0.00	0.00	0.00	0.00	0.01	0.00	0.00	0.00	0.00	0.00	0.00
	0.04	0.04	0.05	0.00	0.00	1.44	1.53	1.51	2.65	0.95	0.97
	0.00	0.00	0.00	0.00	0.00	0.01	0.00	0.01	0.01	0.03	0.01
	0.03	0.03	0.04	0.00	0.00	0.88	0.87	0.72	1.91	0.00	0.01
	0.00	0.00	0.00	0.18	0.00	0.00	0.00	0.00	0.01	0.00	0.00
	0.18	0.19	0.23	0.84	0.02	0.03	0.01	0.01	0.00	0.00	0.00
	0.77	0.75	0.71	0.00	0.99	0.89	0.91	0.92	0.00	0.00	0.00
	0.00	0.00	0.00	0.00	0.00	0.00	0.00	0.00	0.00	0.00	0.00
	7.00	7.00	7.00	5.00	5.00	8.00	8.00	8.00	10.00	2.00	2.00
						0.38	0.36	0.32	0.42		
				0.18	0.00						

				Biotite			
23/1. Matrix		2/1. Matrix	6/1. Matrix	10/1. Matrix	11/1. Matrix	16/1. Matrix	22/1. Matrix
45.75		37.60	35.16	35.79	35.33	35.01	35.33
0.29		1.02	1.67	1.27	1.55	1.13	1.85
0.04		0.01	0.05	0.00	0.02	0.01	0.01
34.86		20.15	19.70	19.50	20.21	19.93	20.44
2.31		19.14	20.47	22.18	21.12	21.92	20.08
0.03		0.09	0.14	0.19	0.20	0.31	0.15
0.82		7.45	7.39	6.81	6.59	7.04	5.98
0.01		0.19	0.09	0.17	0.22	0.23	0.29
0.73		0.11	0.24	0.19	0.24	0.19	0.27
9.56		6.08	8.44	7.72	8.24	8.17	7.04
0.00		0.00	0.00	0.00	0.00	0.00	0
94.40		91.84	93.35	93.82	93.72	93.94	91.44
	11O						
3.08		3.09	2.83	2.89	2.85	2.82	2.93
0.01		0.06	0.10	0.08	0.09	0.07	0.12
0.00		0.00	0.00	0.00	0.00	0.00	0.00
2.77		1.95	1.87	1.86	1.92	1.89	2.00
0.00		0.00	0.00	0.00	0.00	0.00	0.00
0.13		1.31	1.38	1.50	1.42	1.47	1.39
0.00		0.01	0.01	0.01	0.01	0.02	0.01
0.08		0.91	0.89	0.82	0.79	0.84	0.74
0.00		0.02	0.01	0.01	0.02	0.02	0.03
0.09		0.02	0.04	0.03	0.04	0.03	0.04
0.82		0.64	0.87	0.80	0.85	0.84	0.74
0.00		0.00	0.00	0.00	0.00	0.00	0.00
7.00		8.00	8.00	8.00	8.00	8.00	8.00
		0.41	0.39	0.35	0.36	0.36	0.35